Lock-on of vortex shedding to a pair of synthetic jets with phase difference

Chenglei Wang

*Department of Mechanical Engineering, The Hong Kong Polytechnic University, Kowloon,
Hong Kong SAR, China
and School of Mechanical and Aerospace Engineering, Nanyang Technological University,
Singapore 639798, Republic of Singapore*

Hui Tang[*]

*Department of Mechanical Engineering, The Hong Kong Polytechnic University,
Kowloon, Hong Kong SAR, China*

Simon C. M. Yu

Singapore Institute of Technology, Singapore 179104, Republic of Singapore

Fei Duan

*School of Mechanical and Aerospace Engineering, Nanyang Technological University,
Singapore 639798, Republic of Singapore*

This paper furthers our understanding of lock-on that is induced by periodic external forcing. The effect of forcing phase difference is investigated. An extended linear theory is proposed to predict the centers of various lock-on regimes, including harmonic, subharmonic, and superharmonic lock-on, in a parametric map spanned by the forcing frequency and phase difference. It reveals that when the forcing frequency is equal to the natural vortex shedding frequency or its integer multiple, harmonic or subharmonic lock-on occurs at particular forcing phase differences, whereas when the forcing frequency is a submultiple of the natural shedding frequency, superharmonic lock-on occurs. To confirm this theory and also further determine the shape and size of each lock-on regime, a series of numerical simulations is conducted on a circular-cylinder flow system with periodic external forcing being realized by a pair of synthetic jets (SJs). At a Reynolds number 100 and under moderate SJ forcing, five lock-on regimes are captured, including the primary, secondary, tertiary, and first- and second-superharmonic lock-on. It is found that these lock-on regimes are generally in a rhomboidal shape, and their size gradually reduces when the SJ frequency is away from the natural vortex shedding frequency. With these simulations, the aerodynamic forces and wake formation in each lock-on regime are analyzed and compared, with the discussion being focused on the effects of SJ frequency and phase difference. Furthermore, stability analysis is conducted to reveal more flow physics related to lock-on.

I. INTRODUCTION

Lock-on, also known as lock-in [1] or vortex synchronization [2,3], is a complex nonlinear phenomenon where vortex shedding from bluff bodies, typically a circular cylinder, coincides or resonates either with the body's flow-induced vibration (hence called "passive" lock-on in this paper) or with periodic external forcing (hence called "active" lock-on) [4,5]. Passive lock-on widely exists in nature as well as in many engineering applications, which is usually accompanied with rich flow

---

*h.tang@polyu.edu.hk

physics such as flow separation, vortex shedding, vortex-structure interaction, and generation of aerodynamic forces. Hence it has been extensively studied for decades, for which Williamson and Govardhan [6] and Sarpkaya [7] have given good reviews.

Active lock-on can occur when a small amount of energy is injected into the flow system in the form of periodic external forcing. It can bring many benefits, including flow separation control [8], drag reduction [9], lift enhancement [10], suppression of flow-induced vibrations [11], and mixing enhancement. Furthermore, for the purpose of flow control, active lock-on can result in simpler wake dynamics with much less frequency components, making the control much easier [12]. As such, it is important to investigate active lock-on and its characteristics.

In active lock-on, the natural vortex shedding frequency can be attracted or entrained to the frequency of external forcing if these two frequencies are not too different. In this case, the lock-on is called "harmonic" or "primary" lock-on. If the frequency difference is large enough, lock-on does not happen in general and the cylinder may experience quasiperiodic or chaotic oscillations [13]. However, the attraction of frequency can still occur when the ratio of the forcing frequency to the natural vortex shedding frequency is in the vicinity of an integer or the reciprocal of an integer. Under this condition, the vortex shedding frequency can be attracted to a frequency that is a submultiple or an integer multiple of the forcing frequency. In such cases, the lock-on is called "subharmonic" or "superharmonic" lock-on, respectively [14]. Furthermore, in subharmonic lock-on if the vortex shedding frequency is attracted to a half or a third of the forcing frequency, the corresponding lock-on is usually referred to as "secondary" or "tertiary" lock-on, respectively.

Periodic external forcing in active lock-on is usually realized through two types of active-flow-control technologies, i.e., the cylinder's prescribed oscillations and fluidic perturbations. The former includes the cylinder's rotational oscillation [11,13–17] as well as translational oscillation in the transverse direction [1,18–21] and in the streamwise direction [20,22–25], whereas the latter includes fluidic perturbations imposed in the transverse direction [26] and in the streamwise direction [2,4,27–29]. Primary lock-on was observed when the cylinder underwent transverse or rotational oscillation, or when transverse fluidic perturbation was introduced, both at a frequency close to the natural vortex shedding frequency. Stansby [18] and Baek *et al.* [14] further identified the tertiary lock-on when the cylinder transversely or rotationally oscillated in the vicinity of three times the natural shedding frequency. However, the same types of lock-on were not observed when the cylinder underwent streamwise oscillation or when streamwise fluidic perturbation was introduced. Instead, secondary lock-on happened in these cases.

Active lock-on is also affected by the amplitude of external forcing. In general, a lock-on regime (a frequency range in which a specific lock-on occurs) increases with the forcing amplitude [3,12]; meanwhile, more lock-on types and regimes can be attained [25,30]. If the amplitude is too large, however, the forcing can completely suppress the natural vortex shedding, regardless of the frequency. This case was treated as the primary lock-on in some studies, which may not be appropriate because the flow is entirely dominated by the forcing, and hence the actual interaction between the forcing and the vortex shedding is very little.

In addition to the forcing frequency and amplitude, some other forcing parameters, such as the forcing position [12,31], forcing directions [12,22], and forcing waveforms [30], have also been investigated. However, a very important factor that can also affect active lock-on has not been reported in literature, i.e., the phase difference of external forcing. For a circular cylinder immersed in a horizontal flow, this parameter can be defined as the phase difference between the forcing pair exerted over the cylinder's two half surfaces that are divided by the cylinder's streamwise centerline [25]. The forcing pair is said to be in phase when they are symmetric about the cylinder's streamwise centerline, and antiphase when they are antisymmetric. Applying this definition to existing types of forcing gives a forcing phase difference π (i.e., in antiphase) for cylinders undergoing transverse or rotational oscillations and for cylinders with transverse fluidic perturbation, and a forcing phase difference 0 (i.e., in phase) for cylinders undergoing streamwise oscillations and for cylinders with streamwise fluidic perturbation. To our best knowledge, active lock-on with forcing phase differences other than these two values has not been touched on yet.

Therefore, in the present work we aim to investigate the effect of the forcing phase difference on the characteristics of active lock-on, and to remap different lock-on regimes over a wide range of forcing frequencies by adding this new dimension. To realize the variation of forcing phase difference, a pair of synthetic jets (SJs), also called zero-net-mass-flux jets, is implemented on the upper and lower sides of a circular cylinder, each operating independently. Although the use of SJ concept is not new in lock-on studies, unlike in Munday and Taira [12] where a SJ pair operates in antiphase and in Feng and Wang [3] where a single SJ is implemented in the cylinder's mean rear stagnation point, in the present study the forcing phase difference between the SJ pair is allowed to vary from 0 to π. An extended linear theory is proposed to predict the centers of different lock-on regimes. Then a systematic numerical study is conducted at a fixed Reynolds number 100 to determine the shape and size of each lock-on regime, and to compare the aerodynamics and wake formation among different cases. Furthermore, stability analysis is conducted to quantify the change in wake instability due to the operation of the SJ pair in lock-on regimes.

This paper is organized as follows: Section II defines the problem, proposes the extended linear theory, describes the numerical method, and summarizes the simulation cases. Section III gives an overview of the results, including a new parametric map for all lock-on regimes and a summary of aerodynamic forces experienced by the cylinder. In Sec. IV the influence of frequency and phase difference of the SJ pair on the cylinder wake in various lock-on regimes are revealed and compared. In Sec. V stability analysis is performed to reveal more flow physics associated with lock-on. This paper is finally concluded in Sec. VI.

II. PROBLEM DESCRIPTION AND METHODOLOGY

A. Problem description

In this study, a circular cylinder is fixed in a uniform flow, at a low cylinder-diameter-based Reynolds number, i.e., Re = 100. Under this condition, a two-dimensional Kármán vortex street forms behind the cylinder [32]. To investigate the SJ-induced lock-on phenomena, a pair of SJs is implemented on the leeward side of the cylinder, symmetrical about the cylinder's horizontal centerline with an azimuthal angle (γ), as shown in Fig. 1. Although the forcing waveform influences the occurrence of lock-on [30], in this study only the simple harmonic waveform is adopted for the SJ pair. Assuming that the SJ pair operates at the same oscillating frequency (f_{sj}) and velocity amplitude (U_{sj}), the time-dependent velocities of the upper and lower SJs ($\boldsymbol{u}_{sj}^{u}$ and $\boldsymbol{u}_{sj}^{l}$) can be predefined as

$$\boldsymbol{u}_{sj}^{u} = U_{sj} \sin(2\pi f_{sj}t + \phi_u)(\cos\beta, \sin\beta), \tag{1}$$

$$\boldsymbol{u}_{sj}^{l} = U_{sj} \sin(2\pi f_{sj}t + \phi_l)(\cos\beta, -\sin\beta), \tag{2}$$
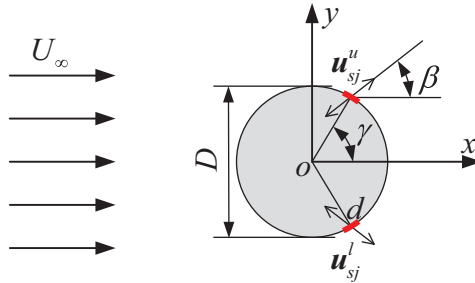

FIG. 1. Schematic of a circular cylinder equipped with a SJ pair. The two short red line sections represent the SJ pair; U_∞ is the freestream velocity; D the cylinder diameter; d the SJ width; β the orientation angle of the SJs; γ azimuthal angle of the SJs; $\boldsymbol{u}_{sj}^{u}$ and $\boldsymbol{u}_{sj}^{l}$ the velocities of the upper and lower SJs, respectively.

where β is the jet orientation angle defined relative to the cylinder's horizontal centerline. ϕ_u and ϕ_l are the operating phase angles of the upper and lower SJs, respectively, from which a phase difference between these two SJs ($\Delta\phi$) can be defined as

$$\Delta\phi = \phi_l - \phi_u. \tag{3}$$

Normalizing f_{sj} using the cylinder's natural vortex shedding frequency (f_n) gives a nondimensional SJ excitation frequency

$$f_{sj}^* = \frac{f_{sj}}{f_n}. \tag{4}$$

The SJ strength is quantified by a momentum coefficient (C_μ) as

$$C_\mu = \frac{2U_{sj}^2 d}{U_\infty^2 D}, \tag{5}$$

where U_∞ is the freestream velocity, D the cylinder diameter, and d the width of SJ slots. In this study, d is set as $1/72$ of the cylinder perimeter, i.e., $d = \pi D/72$.

The aerodynamic forces experienced by the cylinder are assessed using lift and drag coefficients:

$$C_L = \frac{2F_L}{\rho U_\infty^2 D}, \tag{6}$$

$$C_D = \frac{2F_D}{\rho U_\infty^2 D}, \tag{7}$$

where F_L and F_D are the lift and drag forces, respectively, and ρ is the fluid density.

B. Lock-on criterion

In this study we propose our criterion for lock-on as follows: *For a fixed cylinder generating Kármán vortices and undertaking periodic external forcing, lock-on occurs when the cylinder's vortex shedding frequency shifts from its natural value $f^* = f/f_n = 1$ to a neighboring value that is a harmonic, subharmonic or superharmonic of the forcing frequency.* The lock-on is called *Primary Lock-on* when the new vortex shedding frequency is equal to the forcing frequency, *Subharmonic Lock-on* when the new vortex shedding frequency is a submultiple of the forcing frequency, and *Superharmonic Lock-on* when the new vortex shedding frequency is an integer multiple of the forcing frequency. Note that an exception should be given to some special cases where the forcing frequency is the exact integer multiple or submultiple of the natural frequency. In these cases, lock-on still occurs, but the cylinder's vortex shedding frequency remains at $f^* = 1$.

To demonstrate these lock-on phenomena, several representative cases are shown in Fig. 2, in which the frequency spectra of cylinder's lift coefficient (C_L) are used to determine the occurrence of lock-on since the vortex shedding process is closely correlated with the lift variation. It is seen that a single C_L spectrum peak right located at $f^* = 1$ appears in the unforced case [Fig. 2(a)], whereas multiple peaks appear in all the other cases. In the primary lock-on case [Fig. 2(b)], the vortex shedding frequency is attracted to the SJ frequency $f_{sj}^* = 1.1$. In the subharmonic (secondary) lock-on case shown in Fig. 2(c), the SJ pair operates at $f_{sj}^* = 2.1$, causing a shift of the vortex shedding frequency to a half of the SJ frequency, i.e., $f^* = 1.05$. On the contrary, in the superharmonic lock-on case when the SJ pair operates at $f_{sj}^* = 0.54$, the vortex shedding frequency is attracted to a value twice the SJ frequency, i.e., $f^* = 1.08$, as shown in Fig. 2(d). When lock-on does not happen, as shown in Fig. 2(e), the vortex shedding frequency remains at $f^* = 1$, which does not seem to be affected by the SJ operation at $f_{sj}^* = 1.5$.
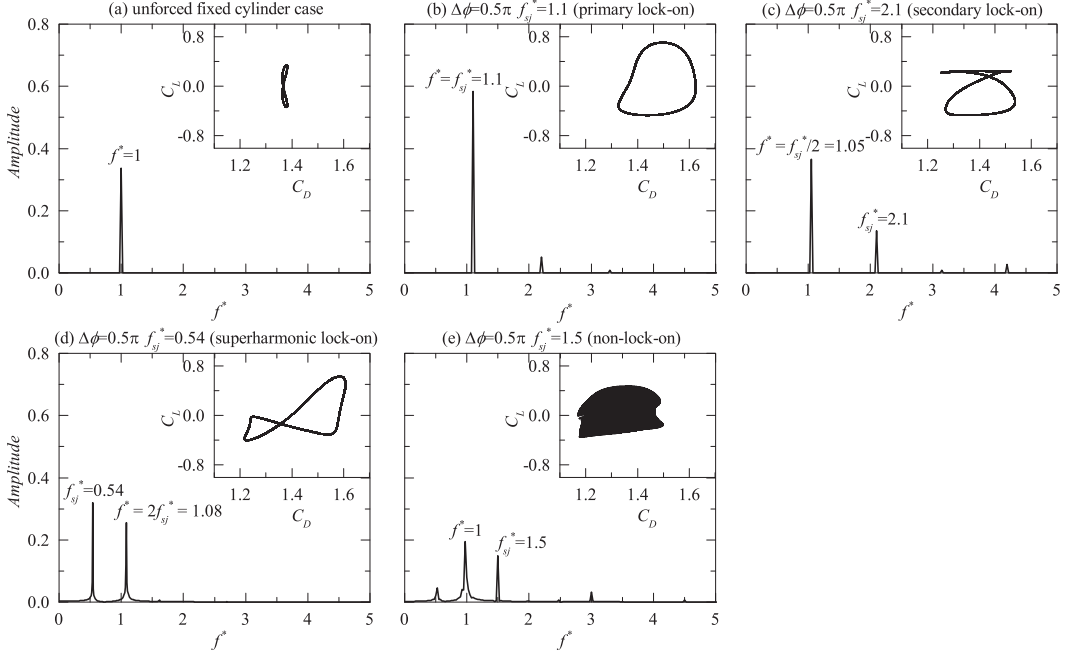
FIG. 2. C_L frequency spectra and C_L-C_D phase diagram of (a) the unforced case and representative (b) primary lock-on, (c) secondary lock-on, (d) superharmonic lock-on, and (e) non-lock-on cases.

In addition to the C_L spectrum, the C_L-C_D phase diagram is also used to determine the occurrence of lock-on. It is seen in the unforced and all the lock-on cases that the phase diagram appears as a nice closed curve, whereas in the non-lock-on case it becomes disordered and unclosed.

C. Extended linear theory

Although lock-on induced by periodic external forcing is a nonlinear synchronization phenomenon, Leontini *et al*. [25] proposed a useful linear model to explain and predict its occurrence in cases where a cylinder oscillates along the streamwise or transverse direction. Different from their work, in the present study the occurrence of lock-on is due to the forcing introduced by a pair of SJs. However, it is still expected that their linear model can be extended to predict the occurrence of lock-on by considering both the SJ pair's phase difference ($\Delta\phi$) and frequency (f_{sj}^*).

According to Leontini *et al*. [25], a two-dimensional flow has the spatio-temporally symmetric property if "evolution forward in time by half a period plus reflection in space about the wake centerline gives the same flow." In this study, the spatio-temporal symmetry of the natural Kármán vortex street behind a fixed cylinder is described as

$$u(x,y,t) = u\left(x, -y, t + \tfrac{1}{2}T_n\right),\tag{8}$$

where T_n is the vortex shedding period. Note that in Eq. (8) the spatio-temporal symmetry is defined based on the streamwise velocity of the flow field (u).

On the other hand, the flow field induced by the SJ pair also has *quasi* spatio-temporal symmetry due to the phase difference ($\Delta\phi$)

$$u_{sj}(x,y,t) = u_{sj}\left(x, -y, t - \frac{y}{|y|}\frac{\Delta\phi}{2\pi}T_{sj}\right),\tag{9}$$

where $T_{sj} = 1/f_{sj}$ is the SJ forcing period. Note that the SJ pair satisfies the spatio-temporal symmetry only when $\Delta\phi = \pm\pi$.

SJ-induced lock-on occurs when the above two flow fields [Eqs. (8) and (9)] are *synchronized*:

$$\frac{1}{2}T_n = -\frac{y}{|y|}\frac{\Delta\phi}{2\pi}T_{sj}.$$

(10)

By applying Eq. (4) and also considering nearby cycles in the synchronization, linear relations between $\Delta\phi$ and f_{sj}^* can be obtained when lock-on occurs:

$$-\frac{\Delta\phi}{2\pi} = \left(N_1 + \frac{1}{2}\right)f_{sj}^* - N_2 \qquad \text{(for } y > 0\text{)},$$

(11)

$$\frac{\Delta\phi}{2\pi} = \left(N_3 + \frac{1}{2}\right)f_{sj}^* - N_4 \qquad \text{(for } y < 0\text{)},$$

(12)

where N_1 and N_3 represent the nearby number of vortex shedding cycles, and N_2 and N_4 represent the nearby number of SJ forcing cycles. $\Delta\phi$ and f_{sj}^* can then be obtained by solving a system of linear Eqs. (11) and (12):

$$f_{sj}^* = \frac{N_2 + N_4}{N_1 + N_3 + 1}, \qquad \frac{\Delta\phi}{\pi} = \frac{2N_2N_3 - 2N_1N_4 + N_2 - N_4}{N_1 + N_3 + 1}.$$

(13)

Although Eq. (13) gives a necessary condition for lock-on, it does not mean that the SJ pair operating at all these $\Delta\phi$ and f_{sj}^* would result in lock-on. It is also hypothesized that lock-on occurs only when the external forcing frequency or any of its harmonics or subharmonics is close to the natural vortex shedding frequency, so that the attraction or entrainment process becomes possible. This implies that the SJ forcing frequency (f_{sj}^*) needs to be either an integer or the reciprocal of an integer

$$f_{sj}^* = \ldots 1/4, 1/3, 1/2, 1, 2, 3, 4 \ldots.$$

(14)

Through the above analysis, therefore, an extended linear theory is obtained: the SJ-induced lock-on happens when the SJ pair's phase difference ($\Delta\phi$) and frequency (f_{sj}^*) satisfy the conditions given by Eqs. (13) and (14). The discrete $\Delta\phi$-f_{sj}^* values predicted by this linear theory are plotted in a $\Delta\phi$-f_{sj}^* map, which will be shown and discussed later in Sec. III A together with the simulation results. Note that these discrete values predicted by the linear theory only represent the centers of various lock-on regimes. Whether their nearby values belong to the respective regimes depends on the strength of the SJ forcing and hence the strength of nonlinear attraction. As such, although very useful, the present linear theory is not able to predict the shape and size of lock-on regimes.

D. Numerical method

In this study, a lattice Boltzmann method (LBM) based numerical framework is adopted, which has been well described and validated in our previous work [31,33,34]. Therefore, it will be briefly introduced in this section.

1. Lattice Boltzmann method

The incompressible D2Q9 MRT LBE model [35], i.e., two-dimensional incompressible multiple-relaxation-time lattice Boltzmann equation model with nine discrete velocities, is employed to simulate the two-dimensional flow around the circular cylinder. The MRT multi-block scheme [36] is applied to enhance the computational efficiency while maintaining sound accuracy. In addition, the interpolated half-way bounce back scheme [37] is incorporated to deal with curved boundaries, and the corrected momentum exchange method [38] is employed for accurate prediction of the aerodynamic forces on the cylinder.

Throughout this study, the computational domain is set as $60D(\text{L}) \times 20D(\text{W})$ with a uniform flow moving from the left to the right with a speed U_∞ as shown in Fig. 3. The circular cylinder is placed in the centerline of the channel and $20D$ away from the inlet boundary. Also, the entire
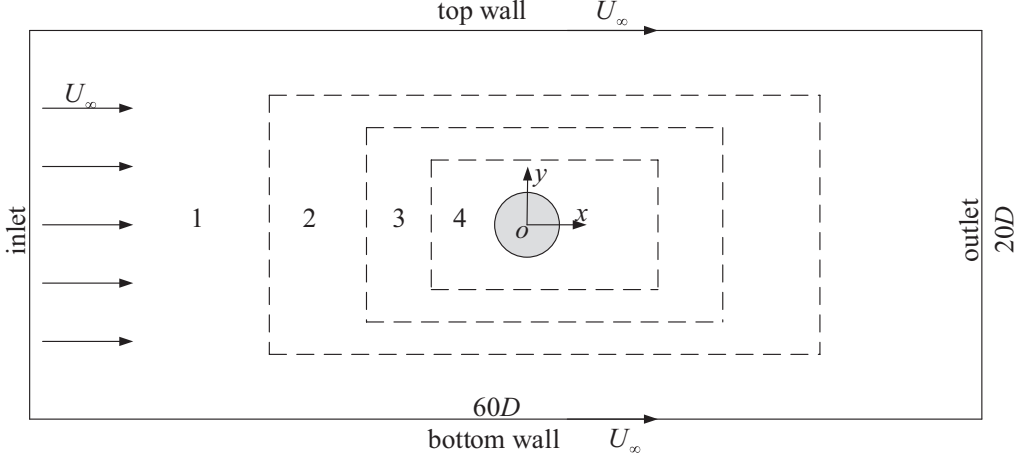
FIG. 3. Computational domain with multiblock arrangement (not in scale). D is the cylinder diameter.

computational domain is divided into four sets of blocks with the mesh density being increased by a factor of 2 as the assigned block number increases. Around the cylinder, the finest block (Block 4) with mesh spacing $\Delta x = D/60$ is used. The velocity of the uniform incoming flow is set as $U/c = 0.01$, corresponding to the nondimensional time step $U_\infty \Delta t / D = 1/6000$, where c is the lattice velocity and Δt the unit time step. The selected mesh and time step are sufficient according to the validation in our previous work [31].

The boundary conditions are also shown in Fig. 3. At the inlet boundary, the nonreflecting inlet boundary condition [39] is used, whereas at the outlet boundary the homogenous Neumann boundary condition is implemented. On the top and bottom walls, the Dirichlet boundary condition is applied with the x-component velocity U_∞ and y-component velocity 0. The SJ actuators are represented by a number of nodes on the cylinder surface, and the time-dependent SJ velocities are realized by enforcing $\boldsymbol{u}_{sj}^u$ and $\boldsymbol{u}_{sj}^l$ on these nodes.

2. Vortex tracking

To quantify the SJ influence on vortex generation and evolution, an algorithm to identify and track vortices based on the λ_{ci} criterion [40] is developed and integrated into the aforementioned numerical framework. The definitions of relevant vortex parameters follow those used in Jardin and Bury [41].

In this study, the nondimensional vorticity (ξ^*) is defined as

$$\xi^* = \frac{\xi D}{U_\infty},\tag{15}$$

where ξ is vorticity. The normalized vortex circulation (Γ^*) can be evaluated as

$$\Gamma^* = \frac{\Gamma}{U_\infty D} = \frac{\iint_{\Sigma_v} \xi \, dx \, dy}{U_\infty D},\tag{16}$$

where Σ_v is the vortex region, whose boundary is identified using isoline of $\lambda_{ci} = 0.2$. In addition, the nondimensional location of the vortex centroid (x_c^*, y_c^*) is determined by

$$x_c^* = \frac{x_c}{D} = \frac{\iint_{\Sigma_v} \xi x \, dx \, dy}{\Gamma D},\tag{17}$$

$$y_c^* = \frac{y_c}{D} = \frac{\iint_{\Sigma_v} \xi y \, dx \, dy}{\Gamma D}.\tag{18}$$

E. Case summary

According to Eqs. (1) to (5), the flow around the cylinder is influenced by the SJ pair through five parameters, i.e., the actuator azimuthal location (γ), the SJ orientation (β), momentum coefficient (C_μ), frequency (f_{sj}^*), and phase difference ($\Delta\phi$). Since the effects of the first three parameters have been well studied in Ongoren and Rockwell [22], Munday and Taira [12], and our previous work [31], they are fixed in the present study as follows: $\gamma = 70°$, meaning that both the actuators are located at about $12°$ upstream of the mean separation point of shear layers; $\beta = 0°$, i.e., the SJs are issued horizontally, so that their forcing along the y direction is avoided; $C_\mu = 0.239$, at which the SJs operate with moderate strength so that they are sufficient to influence but not enough to overwhelm the cylinder wakes [31]. Hence, in this study the focus is only on the effects of the last two parameters, i.e., frequency (f_{sj}^*) and phase difference ($\Delta\phi$). Forty-eight frequency values between 0.2 and 5.1 are selected, covering a large frequency range in which different lock-on phenomena were reported [13,14,25]. At each frequency, five phase difference values varying from 0 to π with an interval of $\pi/4$ are chosen by considering the spatial symmetry of the SJ pair.

The SJ initial forcing conditions, i.e., the actuation timing and starting phase angle, are important for the SJ-based control. Therefore, an investigation has been conducted to study their influence on the resulting flow field before simulating all planned cases. Although not presented here for the sake of brevity, the comparison results revealed that the change of these conditions affects the flow modulation time instead of the final steady-state flow field. Hence in this study the SJ pair in all cases is switched on when the cylinder lift decreasingly approaches its mean value, and, unless stated otherwise, the representing wakes in all cases are shown at this instant.

III. OVERVIEW OF RESULTS

A. Lock-on regimes

Five lock-on regimes, i.e., the primary, secondary, tertiary, as well as first- and second-superharmonic lock-on regimes, are identified through the simulations. Figure 4 shows the distribution of these five regimes in a $\Delta\phi$-f_{sj}^* map, in which the centers of lock-on regimes predicted by the extended linear theory (Sec. II C) are also marked with cross signs. Note that, because of the spatial symmetry of the SJ pair, in this map the data in the upper half ($\pi < \Delta\phi < 2\pi$) are simply mirrored from the lower half. It can be seen that the center of each lock-on regime coincides with the prediction of the linear theory: there are one center in the primary, secondary, and tertiary lock-on regimes at $f_{sj}^* = 1$, 2, and 3, respectively (at $f_{sj}^* = 2$, the two centers appearing at $\Delta\phi = 0$ and 2π are actually the same center due to the periodicity of phase difference), two centers in the first superharmonic lock-on regime at $f_{sj}^* = 1/2$, and three centers in the second superharmonic lock-on regime at $f_{sj}^* = 1/3$. In addition, the centers of the primary and tertiary lock-on regimes are located at $\Delta\phi = \pi$, whereas the center of the secondary lock-on regime is at $\Delta\phi = 0$ or 2π. As for the two superharmonic lock-on regimes, their first centers both fall on a line $\Delta\phi = \pi f_{sj}^*$, and the remaining centers spread along the same $f_{sj}^* = 1/2$ (or $1/3$) line with an increment of π (or $2\pi/3$), which can be further generalized as $2\pi f_{sj}^*$.

It is interesting to see that various lock-on revealed in most of previous studies can be found in this $\Delta\phi$-f_{sj}^* map. When the cylinder undergoes transverse or rotational oscillations, or when transverse fluidic perturbation is introduced, the equivalent forcing phase difference is $\Delta\phi = \pi$, and
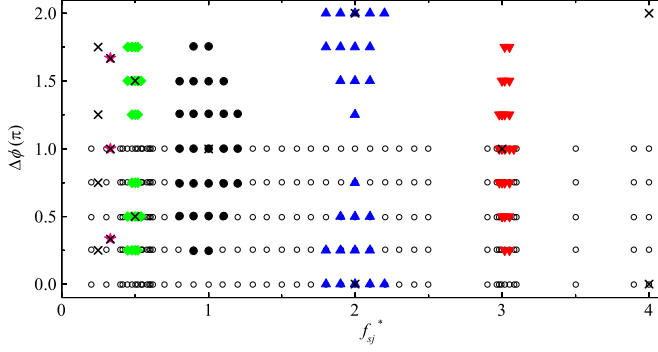
FIG. 4. A $\Delta\phi$-f_{sj}^* map showing the primary, secondary, tertiary, and first- and second-superharmonic lock-on regimes. Solid dark circles (•) represent the primary lock-on cases; solid blue up triangle (▲) the secondary lock-on cases; solid red down triangle (▼) the tertiary lock-on cases; solid green rhombus (♦) the first superharmonic lock-on cases; solid pink star (★) the second superharmonic lock-on cases; open circles (○) the simulated non-lock-on cases; crosses (×) the predicted centers of lock-on regimes based on Eqs. (13) and (14). Note that the data in the upper portion ($\pi < \Delta\phi < 2\pi$) are mirrored from the lower portion ($0 < \Delta\phi < \pi$) due to the symmetry of the SJ pair.

hence the primary or tertiary lock-on, but not the secondary lock-on, occurs [13,14,21,26]. When the cylinder undergoes streamwise oscillations or when streamwise fluidic perturbation is introduced, the equivalent forcing phase difference becomes $\Delta\phi = 0$, and hence only the secondary lock-on occurs [23,28]. In the present study, with the extended linear theory and this $\Delta\phi$-f_{sj}^* map, we are able to identify more lock-on cases in which forcing phase difference is neither 0 nor π. A typical example is the center of the first superharmonic lock-on regime located at $f_{sj}^* = 1/2$ and $\Delta\phi = \pi/2$.

It is also found that, except the second superharmonic lock-on regime, all the lock-on regimes appear in a rhomboidal shape (for the secondary lock-on regime, the two triangles form a rhombus if the periodicity is taken into account). In addition, the size of the rhombus gradually reduces when the SJ frequency is away from 1, indicating the reduced influence of the SJ pair. This explains why the quaternary lock-on regime is not found at $f_{sj}^* = 4$ and the third superharmonic lock-on regime is not found at $f_{sj}^* = 1/4$, which, however, are predicted by the extended linear theory. But it is believed that, with the increase of SJ momentum coefficient, subharmonic or superharmonic lock-on will be captured by the simulations at these two frequencies.

B. Aerodynamic forces

The aerodynamic forces experienced by the cylinder are presented in Fig. 5, including the time-averaged lift and drag coefficients ($\bar{C}_L$ and $\bar{C}_D$) and their standard deviations (σ_{C_L} and σ_{C_D}). All these values are obtained based on the simulation data from 30 vortex shedding periods after the flow fields approach their steady states, which is sufficient to ensure the data convergence. It is seen from Fig. 5(a) that $\bar{C}_L$ deviates from zero when the SJ pair operates near the lock-on frequencies that are either integers or reciprocal of integers, and the extent of the deviation increases when the frequency approaches 1. This indicates that the vortex shedding process is no longer spatio-temporally symmetric when the SJ pair operates in the lock-on regimes, and this asymmetry is positively correlated with the extent of lock-on. If taking a close view at the curves near the primary, secondary, and first superharmonic lock-on frequencies, one can see that the deviation is close to zero when the SJ pair operates either at the center of a lock-on regime or outside the regime, and becomes larger when the SJ pair operates away from the regime center. For example, in the primary lock-on regime near $f_{sj}^* = 1$, $\bar{C}_L$ is close to zero at phase difference $\Delta\phi = 0$ (outside the regime) and π (at the regime center) and increases with the decrease of $\Delta\phi$ between $\pi/4$ and $3\pi/4$.
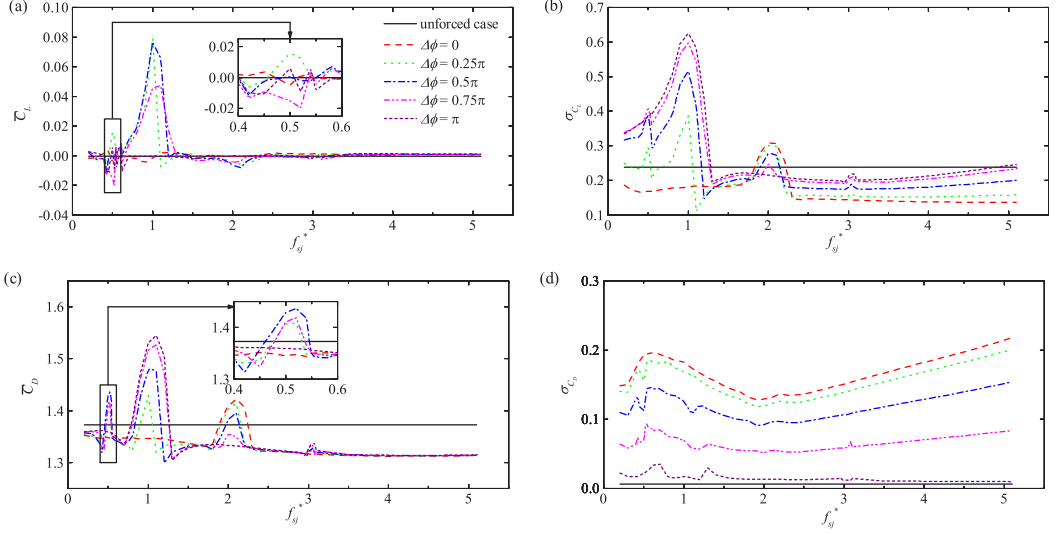
FIG. 5. Time-averaged lift and drag coefficients [(a) $\bar{C}_L$ and (c) $\bar{C}_D$] and standard deviations of lift and drag coefficients [(b) σ_{C_L} and (d) σ_{C_D}] for the cases over a range of f_{sj}^* from 0.2 to 5.1 and $\Delta\phi$ from 0 to π.

Furthermore, by applying symmetry and periodicity to these data with respect to phase difference ($\Delta\phi$), it is found that $\bar{C}_L > 0$ if the SJ pair operates in the lower half portion of each rhomboidal regime, whereas $\bar{C}_L < 0$ if in the upper half portion. This can be directly observed from two curves in the first superharmonic regime near $f_{sj}^* = 1/2$ as shown in the closeup (note the regime center is at $\Delta\phi = \pi/2$): one at $\Delta\phi = \pi/4$ with $\bar{C}_L > 0$, and the other at $\Delta\phi = 3\pi/4$ with $\bar{C}_L < 0$.

The variations of σ_{C_L} against SJ frequency (f_{sj}^*) at various phase differences are shown in Fig. 5(b). It is seen that in general operating the SJ pair at frequencies less or around 1 results in larger lift fluctuations than that in the unforced case ($\sigma_{C_L} = 0.238$), whereas at higher frequencies the lift fluctuations turn smaller. However, the $\Delta\phi = 0$ curve is an exception, which remains significantly smaller values (less than 0.2) throughout the entire investigated range except near $f_{sj}^* = 2$ where the secondary lock-on occurs. This implies that in-phase operation of the SJ pair can reduce the lift fluctuation unless lock-on happens, whereas out-of-phase operation can generally augment the lift fluctuation at frequencies around or less than the primary lock-on frequency. For the latter, the extent of the augmentation increases with the increase of phase difference. Furthermore, it is found that the occurrence of lock-on results in the increase of C_L fluctuation, which is better evidenced by two representative curves: one is the $\Delta\phi = 0$ curve showing only a dramatic increase near $f_{sj}^* = 2$, and the other is the $\Delta\phi = \pi$ curve showing dramatic increases near $f_{sj}^* = 1$ and 3. This is consistent with the observation from Fig. 4: only the secondary lock-on regime contains $\Delta\phi = 0$, and only the first and tertiary lock-on regimes contain $\Delta\phi = \pi$.

It is interesting to see from Fig. 5(c) that the implementation of the SJ pair generally reduces the mean drag ($\bar{C}_D$), regardless of the phase difference. This is because that the two SJs inject nonzero momentum to the downstream and hence produce a nonzero thrust to the cylinder, which offsets some of the main-flow induced drag. However, near the lock-on frequencies, i.e., $f_{sj}^* = 1/2$, 1, 2, and 3, the drag increases dramatically and is even higher than the unforced value ($\bar{C}_D = 1.373$). The increase is the highest at $f_{sj}^* = 1$ and the lowest at $f_{sj}^* = 3$. In addition, in each lock-on regime the increase gradually approaches its maximum when the SJ pair operates towards the regime center.

Unlike the mean drag, the fluctuations of drag (σ_{C_D}) in all cases are greater than that in the unforced case, as shown in Fig. 5(d). Also, since the change of phase difference from in-phase to antiphase makes the momentum generated by the two SJs gradually cancel out each other, the

TABLE I. Seven groups of representative cases selected for the study of cylinder wakes in SJ-pair induced lock-on. Movies are provided for the highlighted cases [42].

Group	$(f_{sj}^*, \Delta\phi)$
Unforced	–
Pri-f_{sj}^*	$\mathbf{(0.8,\pi)}$, $\mathbf{(1,\pi)}$, $(1.2,\pi)$
Pri-$\Delta\phi$	$(1,0.25\pi)$, $\mathbf{(1,0.5\pi)}$, $(1,0.75\pi)$, $\mathbf{(1,\pi)}$
Sec-f_{sj}^*	$(1.8,0)$, $\mathbf{(2,0)}$, $(2.2,0)$
Sec-$\Delta\phi$	$\mathbf{(2,0)}$, $(2,0.25\pi)$, $(2,0.5\pi)$, $(2,0.75\pi)$
Sup-f_{sj}^*	$(0.45,0.5\pi)$, $\mathbf{(0.5,0.5\pi)}$, $(0.54,0.5\pi)$
Sup-$\Delta\phi$	$(0.5,0.25\pi)$, $\mathbf{(0.5,0.5\pi)}$, $(0.5,0.75\pi)$

fluctuation decreases with the increase of phase difference. The lock-on also influences σ_{C_D}, but not as significantly as for the mean drag.

IV. CYLINDER WAKES IN SJ-PAIR INDUCED LOCK-ON

In this section, influence of the SJ pair on the cylinder wakes for seven groups of representative cases is compared and discussed, as summarized in Table I. The unforced case is introduced first as the baseline case. Then cases chosen around the centers of the primary, secondary, and first superharmonic lock-on regimes are presented and compared, with the focus being placed on the effects of SJ frequency (f_{sj}^*) and phase difference ($\Delta\phi$). Furthermore, the change of wakes in various lock-on regimes (cases are highlighted in Table I) is animated in the supplementary movies [42].
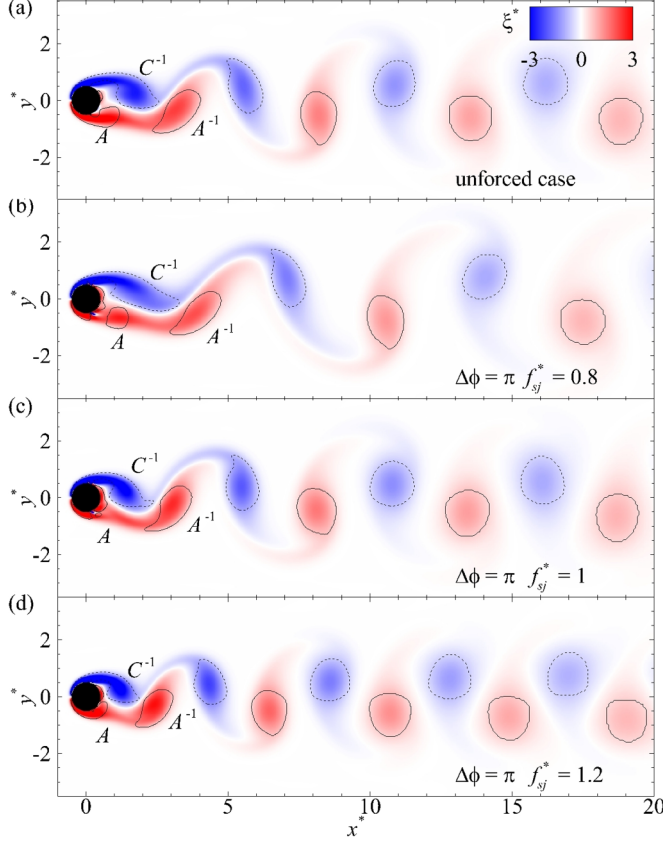
A. Unforced case

In the unforced case, asymmetric vortex shedding occurs on the leeward side of the cylinder, forming a Kármán vortex street, as plotted in Fig. 6(a). The letters "A" and "C" denote the anticlockwise and clockwise vortices enclosed by solid and dashed λ_{ci} isolines, respectively, and the superscript "-1" denotes the vortex generated in the previous period. Under this condition, the cylinder experiences periodic lift fluctuation, whose dominant frequency is $f^* = 1$ as demonstrated in the lift spectrum shown in Fig. 2(a). The variation ranges of the lift and drag coefficients (C_L and C_D), their mean values ($\bar{C}_L$ and $\bar{C}_D$), their standard deviations (σ_{C_L} and σ_{C_D}), and the Strouhal number (defined as St $= f_n D/U_\infty$) are listed in Table II, serving as the baseline values in the present study.

B. Primary lock-on

When the SJ pair operates in the primary lock-on regime as depicted in Fig. 4, the frequency of vortex shedding process can be attracted to the SJ frequency, which has been demonstrated in Fig. 2(b). As a result, the cylinder wake changes accordingly. In addition, the change of SJ phase difference in this regime also affects the wake.

1. Effect of SJ frequency

In the Pri-f_{sj}^* group, the SJ phase difference is fixed at $\Delta\phi = \pi$ and the SJ frequency varies around $f_{sj}^* = 1$. Wake patterns for all three cases are presented in Figs. 6(b) to 6(d). It is seen that the wakes are all spatio-temporally symmetric and very similar to that in the unforced case. But as the frequency increases from 0.8 to 1.2, the duration for the forced vortex shedding process becomes shorter. As such, the streamwise distance between successive vortices gradually decreases, and the vortex just shed from the cylinder (e.g., vortex A^{-1}) reduces in its size and changes in its shape.

FIG. 6. Wake patterns of the unforced case and Pri-f_{sj}^* cases.

Furthermore, the instant at which the wake pattern of the case with $f_{sj}^* = 0.8$ is presented [Fig. 6(b)] coincides with the instant when the upper and lower SJs approach their maximum suction and blowing velocities, respectively. In contrast to vortex C^{-1} which is well connected to the cylinder's upper surface, vortex A is interrupted by the blowing SJ and is disconnected with the cylinder's lower surface. This indicates that the blowing stroke has more influence on the topology of the evolving vortex than the suction stroke.

The evolutions of vortex position and circulation shown in Fig. 7 confirm the spatio-temporal symmetry of the controlled wakes. The trajectory and circulation discontinuities appearing in the near field (i.e., at $x_c^* < 3$) reveal that higher frequency lock-on results in earlier pinch-off and smaller circulation of vortices. Different vortex pinch-off results in different vortex evolution. As such, after the pinch-off the transverse distance between vortices A and C is the largest at the smallest frequency, even though the vortex circulation in all cases becomes almost identical in the far field.

To further investigate the interference of the SJ pair to the vortex shedding process, the variations of lift coefficient (C_L) and the upper and lower SJ velocities (u_{sj}^u and u_{sj}^l) against the lift phase angle (ϕ) are shown in Fig. 8. It is seen that C_L varies almost sinusoidally in all four cases with its mean

TABLE II. Lift and drag data as well as Strouhal number (St) in the unforced case.

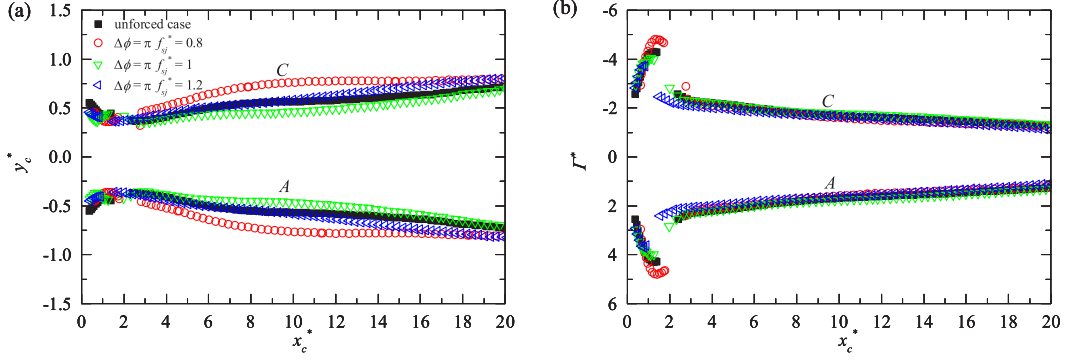| C_L	$\bar{C}_L$	σ_{C_L}	C_D	$\bar{C}_D$	σ_{C_D}	St
± 0.337	0.000	0.238	1.373 ± 0.009	1.373	0.007	0.166

FIG. 7. Evolution of (a) normalized vortex position (y_c^*) and (b) normalized vortex circulation (Γ^*) along the streamwise position (x_c^*) for the Pri-f_{sj}^* cases.

value $\bar{C}_L = 0$, and its oscillation amplitude is the largest at $f_{sj}^* = 1$, consistent with what has been shown in Fig. 5(b). Observations also reveal that the C_L peak is near the instant when vortex A^{-1} is about to shed and vortex A is about to roll up; hence in the following discussions this C_L peak instant is used to define the nominal end of vortex A^{-1} and the nominal start of vortex A.

From Fig. 8 it can be seen that phase differences exist between the two SJ velocity curves and the C_L curve (denoted as $\Delta\phi^u$ and $\Delta\phi^l$ for upper and lower SJs, respectively, as depicted in the plot for the $f_{sj}^* = 0.8$ case), and they vary with the SJ frequency. Similar findings were also reported in lock-on studies on a transversely or rotationally oscillating cylinder [43,44]. The variations of these phase differences are plotted against the SJ frequency in Fig. 9, in which the phase differences are represented by solid symbols, and the phase range of blowing stroke for both SJs are depicted using vertical dashed line segments. It is seen that the $\Delta\phi^u$ curve and the $\Delta\phi^l$ curve are identical, implying that the SJ vortex pairs exert identical influence on the respective two consecutive vortices (i.e., vortices A^{-1} and A or vortices C^{-1} and C whose development is marked with different background colors). As such, only the interference of the lower SJ to vortex A is discussed.

Figure 9(a) shows that $\Delta\phi^l$ linearly decreases with the frequency at a rate of -1.3π. At $f_{sj}^* = 0.8$, the lower SJ starts blowing right after vortex A begins to evolve, and hence it only affects the development of vortex A. Under this condition, the development of vortex A is interrupted by the blowing SJ, as shown in Figs. 10(a1) to 10(a5). At $f_{sj}^* = 1$ and 1.2, the blowing of the lower SJ covers not only the initial stage of vortex A development, but also the late stage of vortex A^{-1} development, as shown in Fig. 9(a). As such, vortex A^{-1} is forced to shed earlier and vortex A starts its main development earlier compared to in the $f_{sj}^* = 0.8$ case, which can be seen from the circulation evolution shown in Fig. 7(b).
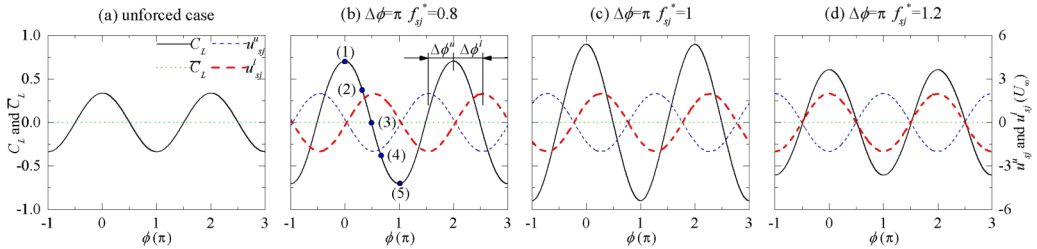

FIG. 8. Variations of the lift coefficient and its time-averaged value (C_L and $\bar{C}_L$) and the upper and lower SJ velocities (u_{sj}^u and u_{sj}^l) against the lift phase angle (ϕ) for the unforced case (a) and Pri-f_{sj}^* cases [(b), (c), and (d)].
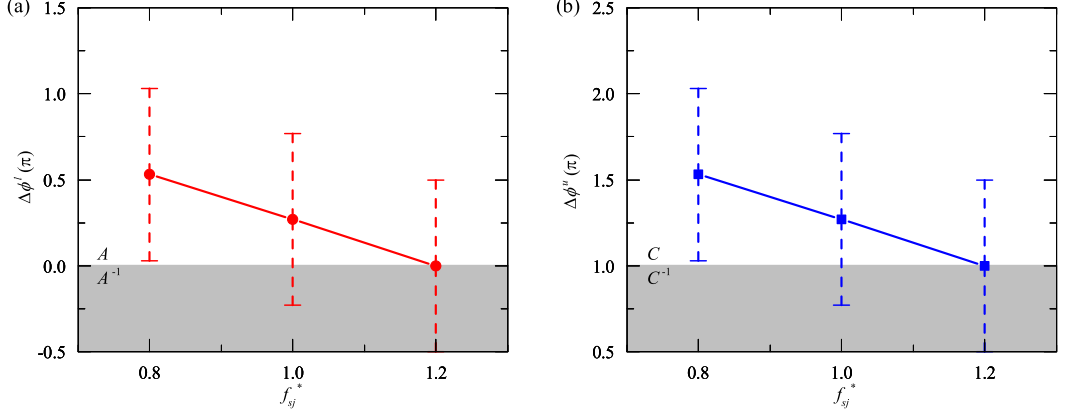
FIG. 9. Variations of (a) $\Delta\phi^l$ (solid red circle ●); (b) $\Delta\phi^u$ (solid blue square ■) with f_{sj}^* for the Pri-f_{sj}^* cases. The vertical dashed lines depict the phase angle ranges of the SJ blowing strokes.

2. Effect of SJ phase difference

In the Pri-$\Delta\phi$ group, the SJ frequency is fixed at $f_{sj}^* = 1$ and the phase difference between the two SJs varies from $\Delta\phi = \pi/4$ to π (note that the case with $\Delta\phi = 0$ is outside the lock-on regime as revealed from Fig. 4). The trajectories of vortex A and vortex C shown in Fig. 11(a) clearly show that the wakes are not spatio-temporally symmetric if the SJ operation is off the lock-on center where $\Delta\phi = \pi$, and the extent of the asymmetry decreases with the increase of $\Delta\phi$. This explains the nonzero $\bar{C}_L$ peaks observed near $f_{sj}^* = 1$ in Fig. 5(a). This asymmetry is also revealed in Fig. 11(b) from the discrepancy in the evolution of vortex A and vortex C circulations in terms of both the locations of vortex pinch-off and the circulation values. As these vortices convect downstream, the unequal circulations are able to further promote the tilting of the wake [45].

The variations of lift coefficient (C_L) and the two SJ velocities (u_{sj}^u and u_{sj}^l) against the lift phase angle (ϕ) are shown in Fig. 12. It can be seen that the C_L curves in all cases vary almost sinusoidally, and their time-averaged values ($\bar{C}_L$) are nonzero (except for the $\Delta\phi = \pi$ case) and decrease with $\Delta\phi$. In addition, the magnitude of C_L variation also increases with $\Delta\phi$, which confirms the trend of the lift standard deviation presented in Fig. 5(b).

The phase differences between the C_L peak and its nearest u_{sj}^l peak ($\Delta\phi^l$) and between the C_L peak and its nearest u_{sj}^u peak ($\Delta\phi^u$) also change with the SJ phase difference ($\Delta\phi$), as shown in Fig. 13. Opposite variation trends are found for $\Delta\phi^l$ and $\Delta\phi^u$. That is, $\Delta\phi^l$ almost linearly decreases, whereas $\Delta\phi^u$ almost linearly increases with increasing $\Delta\phi$. The rate of decrease or increase for both curves is approximately 0.5.
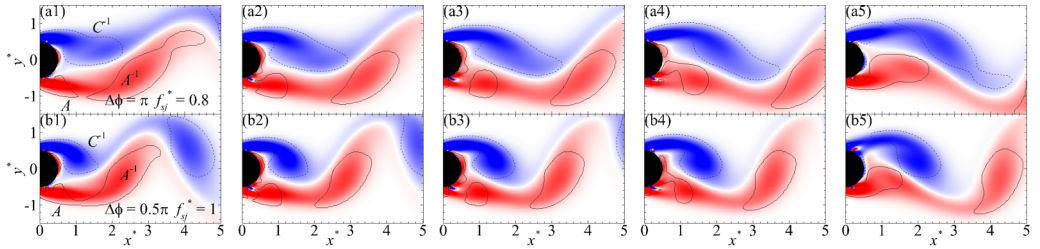

FIG. 10. Instantaneous wake patterns for the $f_{sj}^* = 0.8$ and $\Delta\phi = \pi$ case (a1) to (a5); and the $f_{sj}^* = 1$ and $\Delta\phi = \pi/2$ case (b1) to (b5). The five selected instants for these two cases are indicated by the five points plotted in Figs. 8(b) and 12(c), respectively. This figure reveals that the formation processes of vortices A are similar in these two cases, because of the similar blowing phase angles of the lower SJs.
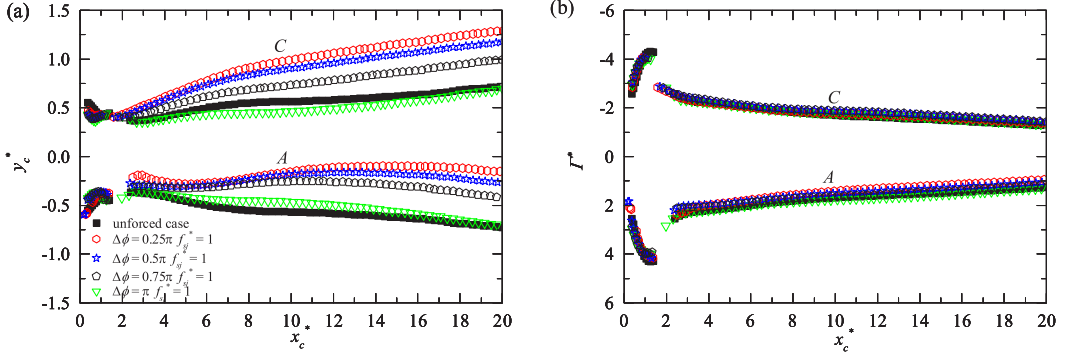
FIG. 11. Evolution of (a) normalized vortex position (y_c^*) and (b) normalized vortex circulation (Γ^*) along the streamwise position (x_c^*) for the Pri-$\Delta\phi$ cases.

When the SJ pair operates at $\Delta\phi = \pi/4$ and $\pi/2$, the blowing of the lower SJ only affects the development of vortex A, as indicated in Fig. 13(a). On the contrary, it affects both the late stage of vortex A^{-1} development and the initial stage of vortex A development at $\Delta\phi = 3\pi/4$ and π. As such, vortex A^{-1} is forced to shed slightly earlier and the development of vortex A is delayed. Different from the lower SJ, the blowing of the upper SJ affects both the late stage of vortex C^{-1} development and the initial stage of vortex C development in all cases, as revealed in Fig. 13(b). Hence in the present case group the evolution of vortex C^{-1} is forced to shed slightly earlier and the development of vortex C is delayed. Furthermore, in each case (except the $\Delta\phi = \pi$ case), the influence of the upper and lower SJs on the vortex shedding process is different, which causes the generation of different vortices in terms of the pinch-off location and circulation and results in tilting wakes.

From the above results it can be concluded that the phase angle of SJ blowing relative to the C_L peak (i.e., $\Delta\phi^l$ or $\Delta\phi^u$) plays an important role in the vortex development and the resulting wake. This can be further confirmed by an observation that similar vortex evolution process can be achieved through applying similar SJ blowing conditions in different cases. For example, the variation of $\Delta\phi^l$ from $f_{sj}^* = 0.8$ to 1.0 in the Pri-f_{sj}^* group [Fig. 9(a)] is similar to that from $\Delta\phi = \pi/2$ to π in the current Pri-$\Delta\phi$ group [Fig. 13(a)]. Specifically, the development of vortex A in the $f_{sj}^* = 0.8$ and $\Delta\phi = \pi$ case is very similar to that in the $f_{sj}^* = 1$ and $\Delta\phi = \pi/2$ case, as revealed in Fig. 10. As a result, the effect of f_{sj}^* on altering the evolution of vortex A in the former cases is very similar to the effect of $\Delta\phi$ in the latter cases in the respective ranges.

C. Secondary lock-on

When the SJ pair operates in the secondary lock-on regime as depicted in Fig. 4, the frequency of vortex shedding process is attracted to a half of the SJ frequency as demonstrated in Fig. 2(c),
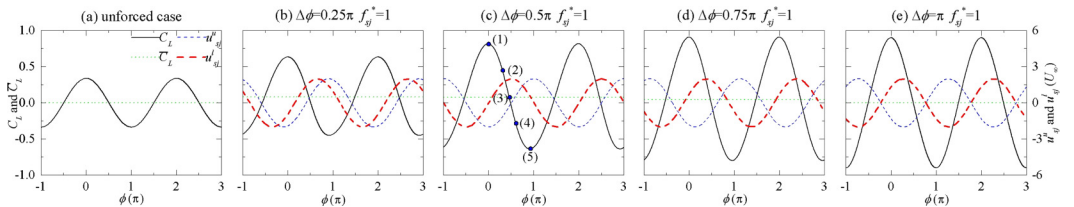

FIG. 12. Variations of the lift coefficient and its time-averaged value (C_L and $\bar{C}_L$) and the upper and lower SJ velocities (u_{sj}^u and u_{sj}^l) against the lift phase angle (ϕ) for the unforced case (a) and Pri-$\Delta\phi$ cases [(b), (c) (d), and (e)].
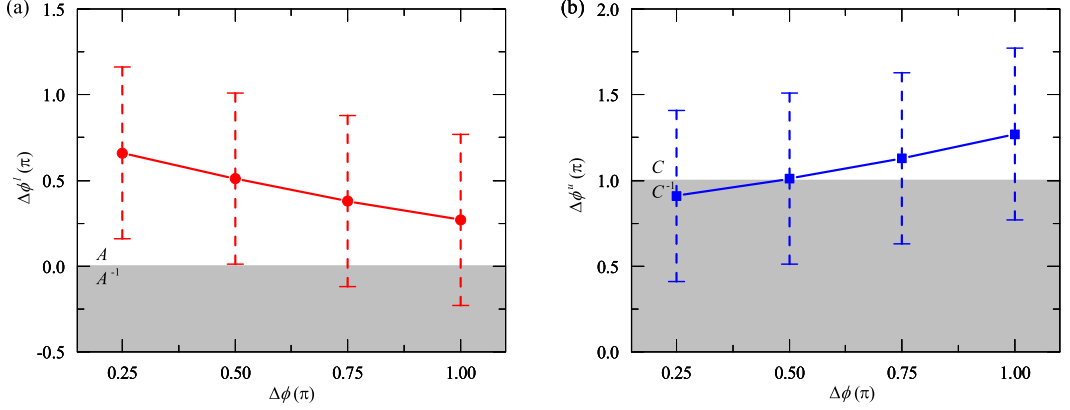
FIG. 13. Variations of (a) $\Delta\phi^l$ (solid red circle ●); (b) $\Delta\phi^u$ (solid blue square ■) with $\Delta\phi$ for the Pri-$\Delta\phi$ cases. The vertical dashed lines depict the phase angle ranges of the SJ blowing strokes.

meaning that the SJ pair affects the vortex shedding process twice in one vortex shedding period. As a result, the cylinder wake becomes more complex than in the primary lock-on regime.

1. Effect of SJ frequency

In the Sec-f_{sj}^* group, the SJ phase difference is fixed at $\Delta\phi = 0$ and the SJ frequency varies around $f_{sj}^* = 2$. Although not presented for brevity, the wakes in the present group are all spatio-temporally symmetric, and the streamwise distance of successive vortices decreases with f_{sj}^*, similar to what has been observed in the Pri-f_{sj}^* group. Figure 14 plots the variations of C_L (lift coefficient) as well as u_{sj}^u and u_{sj}^l (velocities of the upper and lower SJs) against the lift phase angle (ϕ) of all the Sec-f_{sj}^* cases, where all the C_L curves appear in a sinusoidal shape.

The variations of $\Delta\phi^l$ (phase difference between the C_L peak and its nearest u_{sj}^l peak) and $\Delta\phi^u$ (phase difference between the C_L peak and its nearest u_{sj}^u peak) against f_{sj}^* are shown in Fig. 15. In each subfigure, two curves appear, corresponding to two times of blowing in one vortex shedding period. It can be seen that the curves for the lower SJ are identical to those for the upper SJ due to the spatio-temporal symmetry, and all curves decrease nonlinearly with f_{sj}^*. In the $f_{sj}^* = 1.8$ case, the first blowing of the lower SJ starts right before vortex A^{-1} sheds as shown in Fig. 15(a), so it mainly affects the initial stage of vortex A development. As f_{sj}^* gradually increases to 2.2, the first blowing of the lower SJ affects the last quarter of vortex A^{-1} development, and the second blowing affects the second quarter of vortex A development. By considering the periodicity of these processes, it
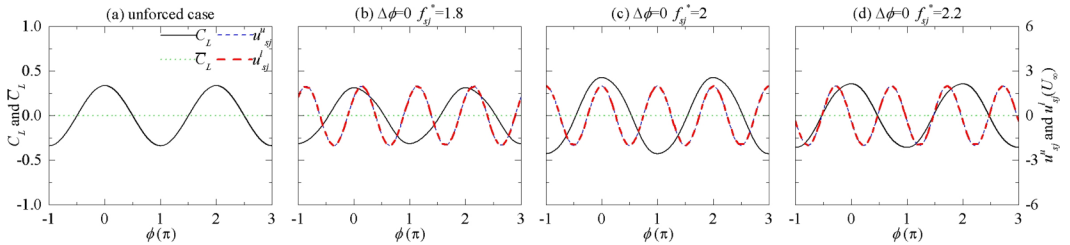

FIG. 14. Variations of the lift coefficient and its time-averaged value (C_L and $\bar{C}_L$) and the upper and lower SJ velocities (u_{sj}^u and u_{sj}^l) against the lift phase angle (ϕ) for the unforced case (a) and Sec-f_{sj}^* cases [(b), (c), and (d)].
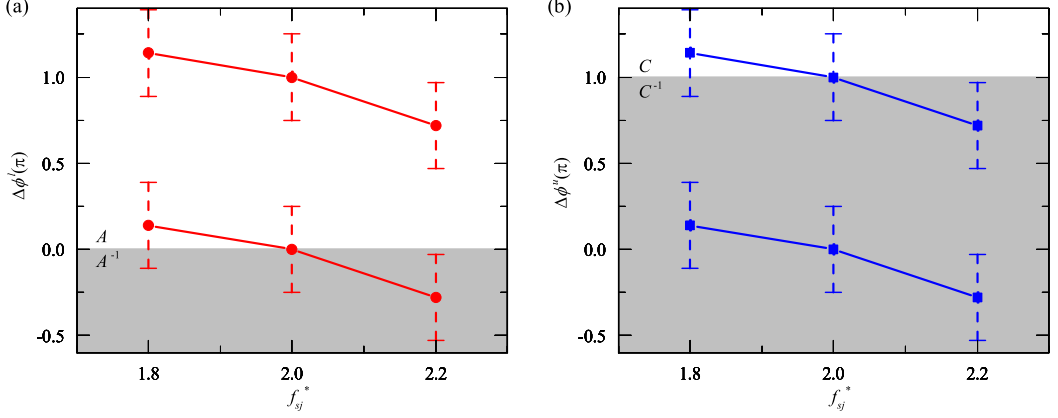
FIG. 15. Variations of (a) $\Delta\phi^l$ (solid red circle ●); (b) $\Delta\phi^u$ (solid blue square ■) with f_{sj}^* for the Sec-f_{sj}^* cases. The vertical dashed lines depict the phase angle ranges of the SJ blowing strokes.

can be deducted that the development of each vortex is firstly interrupted in the second quarter and then forced to shed earlier in the last quarter.

2. Effect of SJ phase difference

In the Sec-$\Delta\phi$ group, the SJ frequency is fixed at $f_{sj}^* = 2$ while the SJ phase difference varies from $\Delta\phi = 0$ to $3\pi/4$. Similar to the Pri-$\Delta\phi$ group, the wakes in the current group cases are not spatio-temporally symmetric if the SJ operation is off the lock-on center where $\Delta\phi = 0$, which is confirmed by the vortex trajectories and circulations plotted in Fig. 16. By comparing Fig. 11(a) with Fig. 16(a), it is interesting to see that although the extent of wake tilting in the Sec-$\Delta\phi$ cases is similar to that in the Pri-$\Delta\phi$ cases, their tilting directions are different: the tilting in the Pri-$\Delta\phi$ cases is towards the upper corner, whereas in the present cases it is towards the lower corner. Furthermore, in the present cases the tilting angle increases with $\Delta\phi$.

Figure 17 shows the variations of lift coefficient (C_L) and SJ velocities (u_{sj}^u and u_{sj}^l) against the lift phase angle (ϕ). Unlike in the previous case groups, the C_L curves in the present group deviate from a sinusoidal shape as $\Delta\phi$ increases. It is further observed that the phase range for the upper portion of the curve ($C_L \geqslant 0$) increases with $\Delta\phi$. In this portion the shape of C_L curve gradually changes from a single-peak one to a double-peak one, whereas in the lower portion ($C_L \leqslant 0$) the
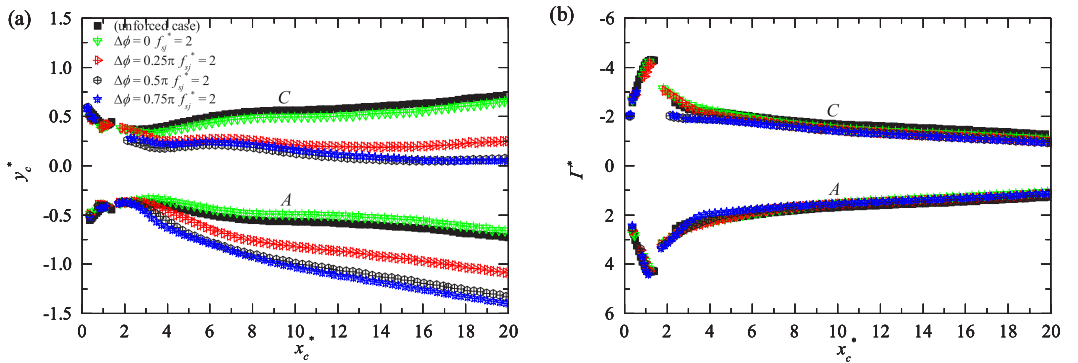

FIG. 16. Evolution of (a) normalized vortex position (y_c^*) and (b) normalized vortex circulation (Γ^*) along the streamwise position (x_c^*) for the Sec-$\Delta\phi$ cases.
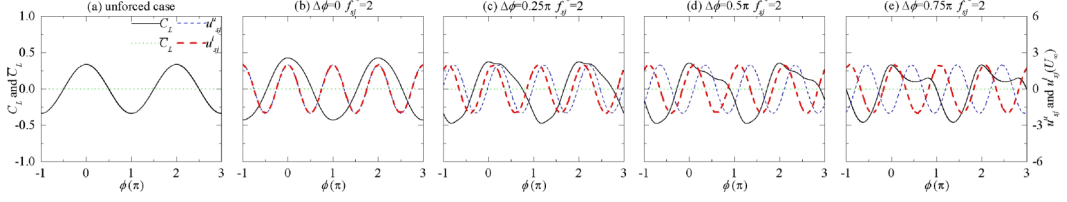
FIG. 17. Variations of the lift coefficient and its time-averaged value (C_L and $\bar{C}_L$) and the upper and lower SJ velocities (u_{sj}^u and u_{sj}^l) against the lift phase angle (ϕ) for the unforced case (a) and Sec-$\Delta\phi$ cases [(b), (c) (d), and (e)].

shape of single-trough C_L curve does not change too much. It is interesting to see that, although the upper and lower C_L portions are quite different, the mean lift ($\bar{C}_L$) in all cases is close to zero, which is different from what has been observed in the Pri-$\Delta\phi$ group.

Figure 18 shows the variation of $\Delta\phi^l$ (phase difference between the C_L peak and its nearest u_{sj}^l peak) and $\Delta\phi^u$ (phase difference between the C_L peak and its nearest u_{sj}^u peak) against $\Delta\phi$. It is seen that the change of $\Delta\phi^l$ (about 0.1π) is much smaller than the change of $\Delta\phi^u$ (about 0.45π), meaning that the change of $\Delta\phi^u$ makes more impact. Since the upper SJ mainly affects the development of vortex C, this indicates that the deviation of the upper portion of C_L curve from an ideal sine wave as revealed in Fig. 17 is mainly caused by the upper SJ and hence by the modification of vortex C.

D. Superharmonic lock-on

When the SJ pair operates in the first superharmonic lock-on regime as depicted in Fig. 4, the frequency of vortex shedding process is attracted to a value twice of the SJ frequency, which has been demonstrated in Fig. 2(d). This means that the SJ pair affects the vortex shedding process once every two vortex shedding periods. Consequently, the cylinder wake repeats every two vortex shedding periods. For the convenience of discussion, in this section the first superharmonic lock-on is simply called the superharmonic lock-on.

1. Effect of SJ frequency

In the Sup-f_{sj}^* group, the SJ phase difference is fixed at $\Delta\phi = \pi/2$ and the SJ frequency varies near $f_{sj}^* = 0.5$. Similar wake patterns are observed in this case group. That is, two successive vortex
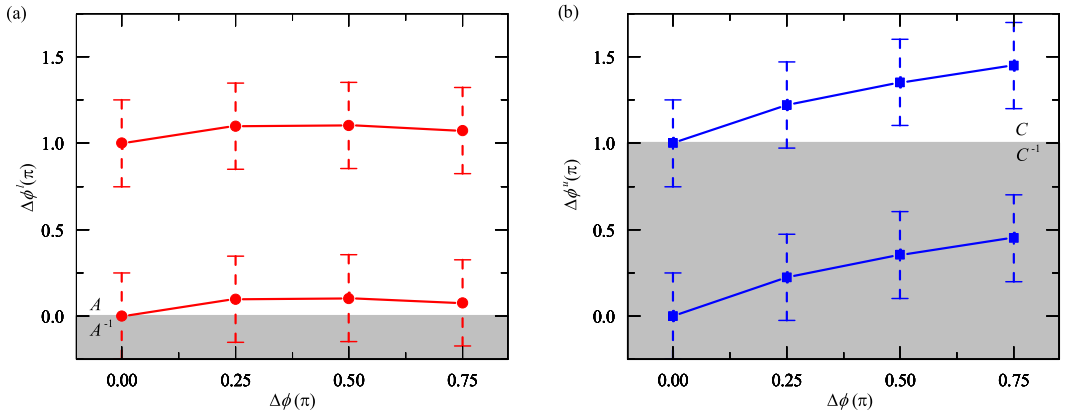

FIG. 18. Variations of (a) $\Delta\phi^l$ (solid red circle ●); (b) $\Delta\phi^u$ (solid blue square ■) with $\Delta\phi$ for the Sec-$\Delta\phi$ cases. The vertical dashed lines depict the phase angle ranges of the SJ blowing strokes.
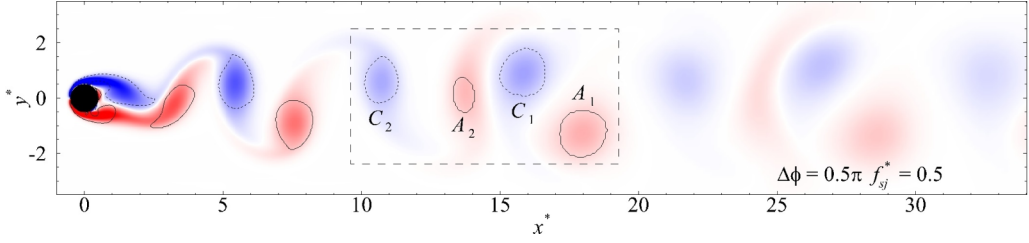
FIG. 19. Wake pattern of the case with $f_{sj}^* = 0.5$ and $\Delta\phi = 0.5\pi$. The box enclosed by dashed lines surrounds the four successive vortices shedding over one wake pattern period. The subscripts "1" and "2" denote vortices shedding in the first and second halves of one wake pattern period, respectively.

pairs are generated in every two vortex shedding periods or in every one SJ operation period. One representative case ($f_{sj}^* = 0.5$ and $\Delta\phi = 0.5\pi$) is shown in Fig. 19, where the first pair A_1 and C_1 and the second pair A_2 and C_2 as enclosed in a box are generally different in shape and size. The trajectories and circulations of the two vortex pairs for the Sup-f_{sj}^* group are quantified in Fig. 20. It can be seen that unlike in the Pri-f_{sj}^* and Sec-f_{sj}^* groups the spatio-temporal symmetry does not hold in the present group.

Figure 21 shows the variations of lift coefficient (C_L) and SJ velocities (u_{sj}^u and u_{sj}^l) against the lift phase angle (ϕ) over one wake pattern period (equivalent to two vortex shedding periods or one SJ operation period). It can be seen that all C_L curves have two sets of peaks and troughs in each wake pattern period. However, neither of them is anti-symmetric. Furthermore, the two vortex shedding processes in each wake pattern period are not evenly distributed in time, which can be seen from the uneven peak-to-peak distance of the C_L curve along the $\Delta\phi$ axis.

The variations of $\Delta\phi^l$ (phase difference between the C_L peak and its nearest u_{sj}^l peak) and $\Delta\phi^u$ (phase difference between the C_L peak and its nearest u_{sj}^u peak) against f_{sj}^* in the Sup-f_{sj}^* cases are shown in Fig. 22. Both $\Delta\phi^l$ and $\Delta\phi^u$ decrease nonlinearly with f_{sj}^*. Although it seems that the upper and lower SJs exert the same influence on respective vortices, they do not result in identical vortex shedding processes and hence spatio-temporally symmetric wake like in the Pri-f_{sj}^* and the Sec-f_{sj}^* groups. This stems from different initial status of the upper and lower vortices when the respective SJ starts the blowing stroke. For example, in the $f_{sj}^* = 0.45$ case, the lower SJ starts blowing at around the lift phase angle $\phi = 5\pi/3$ [see the red dashed line plotted in Fig. 21(b)], where vortex A_1 is alike but smaller than that in the unforced case [compare the red vortices in Figs. 23(a1) and 23(b1)], whereas the upper SJ starts blowing at around $\phi = 8\pi/3$ (see the blue dashed line), where
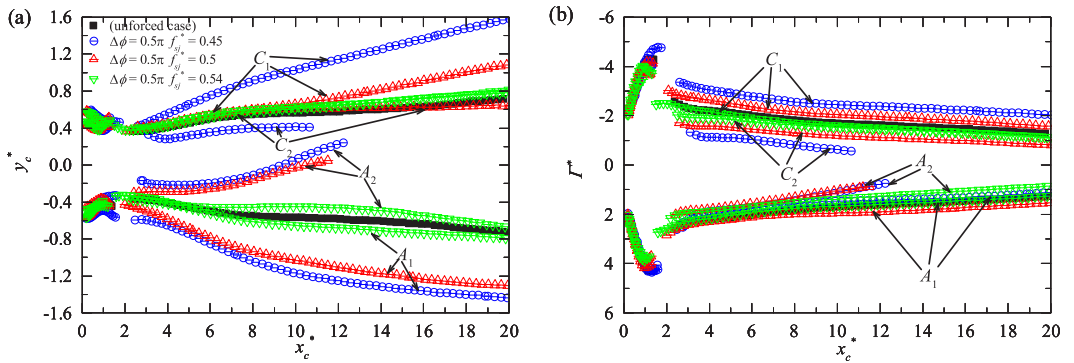

FIG. 20. Evolution of (a) normalized vortex position (y_c^*) and (b) normalized vortex circulation (Γ^*) along the streamwise position (x_c^*) for the Sup-f_{sj}^* cases. A_1, C_1, A_2, and C_2 denote the four representative vortices as shown in Fig. 19.
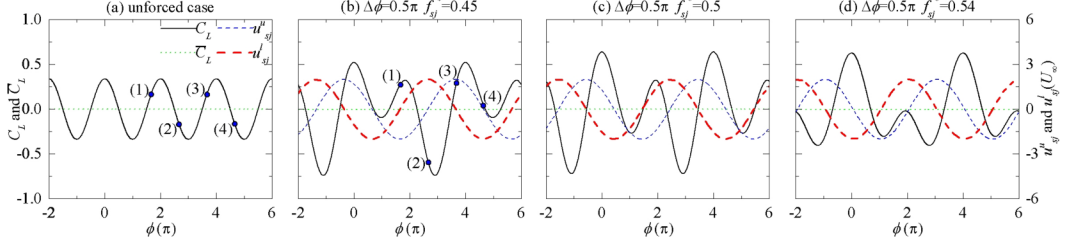
FIG. 21. Variations of the lift coefficient and its time-averaged value (C_L and $\bar{C}_L$) and the upper and lower SJ velocities (u_{sj}^u and u_{sj}^l) against the lift phase angle (ϕ) for the unforced case (a) and Sup-f_{sj}^* cases [(b), (c), and (d)].

vortex C_1 is larger than that in the unforced case [compare the blue vortices in Figs. 23(a2) and 23(b2)]. Since in the unforced case vortex A_1 in Fig. 23(a1) is identical to vortex C_1 in Fig. 23(a2) because of the spatio-temporal symmetry, in the $f_{sj}^* = 0.45$ case vortex A_1 in Fig. 23(b1) is therefore significantly smaller than vortex C_1 in Fig. 23(b2). Hence applying the same SJ to these two vortices results in different vortex evolution processes. This is further confirmed by more different vortices at the end of blowing, i.e., vortex A_2 at $\phi = 11\pi/3$ [Fig. 23(b3)] and vortex C_2 at $\phi = 14\pi/3$ (or $2\pi/3$) [Fig. 23(b4)].

2. Effect of SJ phase difference

In the Sup-$\Delta\phi$ group, the SJ frequency is fixed at $f_{sj}^* = 0.5$ while the SJ phase difference varies from $\Delta\phi = \pi/4$ to $3\pi/4$. Although not shown here for brevity, the wakes and the C_L curves in the present group are similar to those in the Sup-f_{sj}^* group, and they also vary with $\Delta\phi$. Furthermore, the variation trends of $\Delta\phi^l$ and $\Delta\phi^u$ with $\Delta\phi$ are similar to those in the Pri-$\Delta\phi$ group, i.e., $\Delta\phi^l$ decreases with $\Delta\phi$, while $\Delta\phi^u$ increases.

V. STABILITY ANALYSIS

It is known that the vortex evolution behind a fixed circular cylinder is associated with the instability in the wake, and its alteration is usually accompanied with a shift of the wake instability [46,47]. As revealed in Sec. IV, the operation of the SJ pair changes the vortex evolution and resulting wake pattern that appear in the unforced case. Hence it will also change the associated
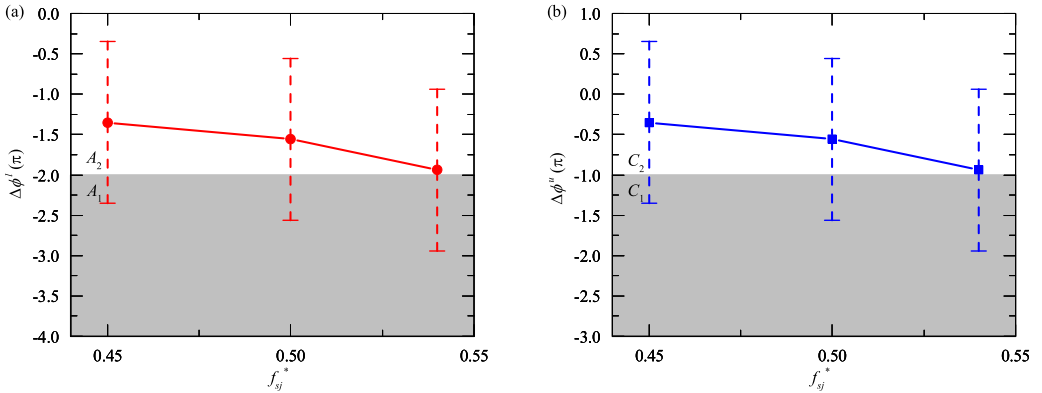

FIG. 22. Variations of (a) $\Delta\phi^l$ (solid red circle ●); (b) $\Delta\phi^u$ (solid blue square ■) with f_{sj}^* for the Sup-f_{sj}^* cases. The vertical dashed lines depict the phase angle ranges of the SJ blowing strokes.
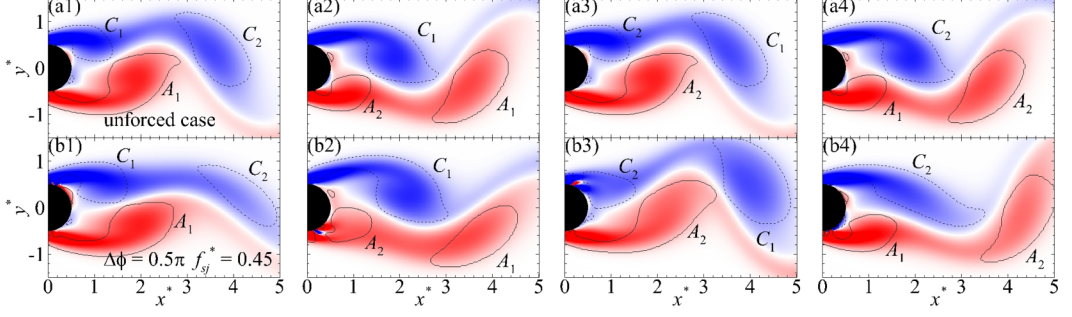
FIG. 23. Instantaneous wake patterns for the unforced case (a1) to (a4); and the $f_{sj}^* = 0.45$ and $\Delta\phi = \pi/2$ case (b1) to (b4). The four selected instants for these two cases are indicated by the four points plotted in Figs. 21(a) and 21(b), respectively.

wake instability. To quantify the latter change in lock-on regimes, in this section we perform the local linear stability analysis. The mean flow instead of the steady base flow is chosen for the analysis, because, according to Sipp and Lebedev [48], the mean flow is stable and its linear dynamics can approximately yield the nonlinear frequency of the limit cycle. Furthermore, the mean flow is assumed to be inviscid and locally parallel downstream of the cylinder, which has been adopted in Triantafyllou *et al.* [46] and Thiria and Wesfreid [49].

Assume the disturbance stream function to be

$$\Psi(x,y,t) = \psi(y)e^{i(kx-\omega t)}, \tag{19}$$

where ψ is the disturbance amplitude, k the complex wave number, and ω the complex frequency. The linear stability properties of a time-averaged flow can be determined by the solutions of the inviscid Orr-Sommerfeld or Rayleigh equation [50]

$$(k\bar{u} - \omega)(\psi'' - k^2\psi) - k\bar{u}''\psi = 0 \tag{20}$$

with boundary conditions $\psi(\pm\infty) = 0$, where $\bar{u}$ is the time-averaged streamwise velocity at a selected downstream location, and the double prime denotes the second derivative with respect to y. Equation (20) defines an eigenvalue problem and yields a dispersion relation $\omega = \omega(k)$. By mapping a number of constant k_i (i.e., the imaginary part of k) lines in the complex ω plane, a "critical point", ω_0, can be identified [50,51]. Its imaginary part, ω_{0i}, is related to the growth rate of disturbance, whose sign determines the nature of wake instability. Specifically, if ω_{0i} is positive, the flow is absolutely unstable, and the disturbance will spread to the entire flow. On the other hand, if ω_{0i} is negative, the flow is convectively unstable, and the disturbance will be swept away with time [47,50,51].

In the time-averaged flow of the unforced case, a recirculation region of a length twice the cylinder diameter appears downstream the cylinder, as represented by the blue region in Fig. 24(a). The linear stability analysis is performed at various downstream locations from $x^* = 0.6$ to 3.13.
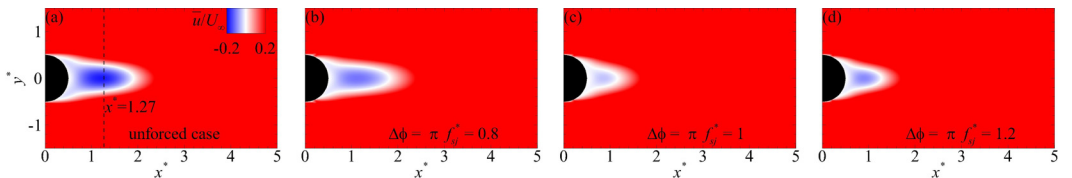

FIG. 24. Contours of time-averaged streamwise velocity ($\bar{u}/U_\infty$) for the unforced case (a) and the Pri-f_{sj}^* cases [(b) to (d)].
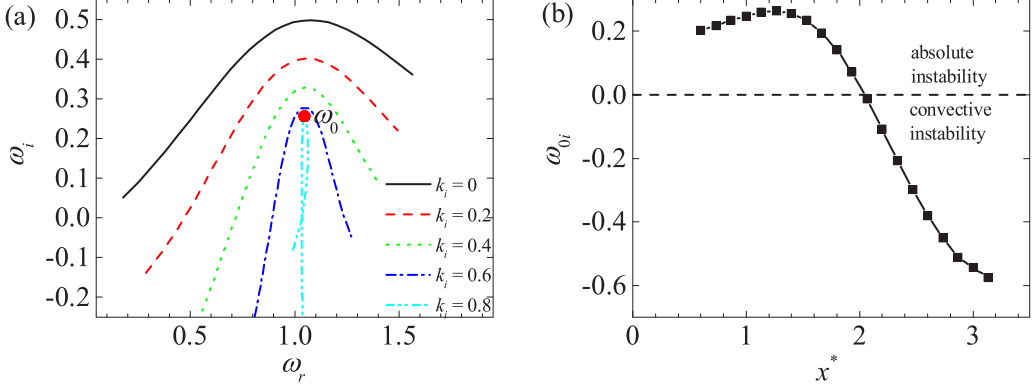
FIG. 25. (a) Constant k_i lines in the ω plane at $x^* = 1.27$ for the unforced case. The "critical point" ω_0 is identified at the edge of a cusplike trajectory. (b) The disturbance growth rate, represented by ω_{0i}, against the streamwise location (x^*) for the unforced case.

At each selected x^*, the "critical point" ω_0 is determined through finding a cusp along a specific k_i line in the ω plane. This is demonstrated in Fig. 25(a), where a number of k_i lines at $x^* = 1.27$ are plotted and ω_0 is identified at the cusp of the $k_i = 0.8$ line. The ω_0 values at other downstream locations can also be determined in a similar way. Figure 25(b) plots ω_{0i}, the imaginary part of ω_0, against x^*. It is seen that ω_{0i} is positive at about $x^* < 2$, i.e., in the recirculation region, while it becomes negative further downstream. This indicates that the flow in the near-wake (recirculation) region is absolutely unstable, which leads to the formation of the vortex street as shown in Fig. 6(a), and the flow becomes convectively unstable in the far-wake region.

Since in the unforced case the absolutely unstable flow is located immediately downstream of the cylinder, it is no doubt that the injection of SJs into this flow region will change the wake stability and the resulting dynamics. This change can be demonstrated in the primary lock-on regime. In the Pri-f_{sj}^* group where the SJ pair operates with $\Delta\phi = \pi$ at various frequencies, as shown in Figs. 24(b)–24(d), the time-averaged recirculation region shrinks towards upstream, in which the strength of reverse flow is also reduced. Such changes are the most prominent when the SJ pair operates at $f_{sj}^* = 1$. Accordingly, the linear stability analysis captures the shrink of absolutely unstable flow region (especially in the $f_{sj}^* = 1$ and 1.2 cases) and the reduction of disturbance growth rate in this flow region [see Fig. 26(a)]. Similarly, in the Pri-$\Delta\phi$ group the operation of the SJ pair also causes the
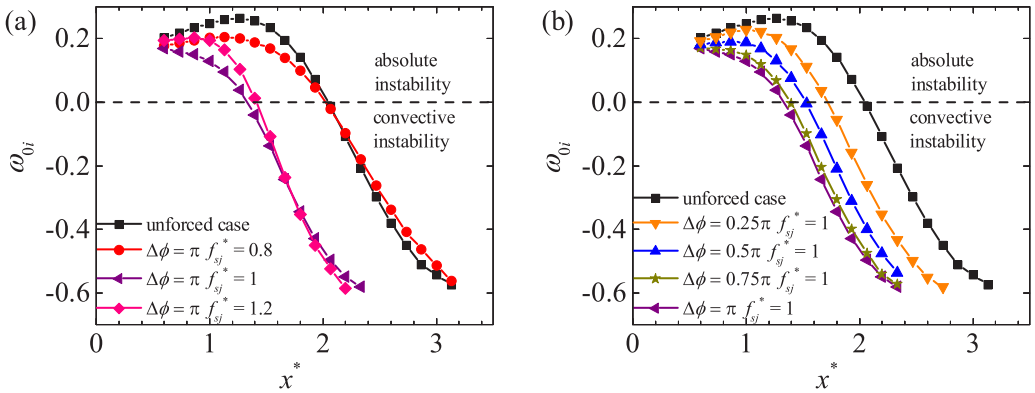

FIG. 26. The disturbance growth rate, represented by ω_{0i}, against the streamwise location (x^*) for the unforced case as well as the Pri-f_{sj}^* cases (a) and the Pri-$\Delta\phi$ cases (b).
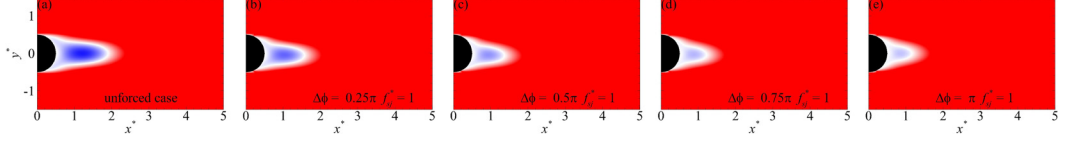
FIG. 27. Contours of time-averaged streamwise velocity ($\bar{u}/U_\infty$) for the unforced case (a) and Pri-$\Delta\phi$ cases [(b) to (e)].

shrink of time-averaged recirculation region and the reduction in the strength of reverse flow, as shown in Fig. 27. The linear stability analysis also confirms the shrink of absolutely unstable flow region and the reduction of disturbance growth rate [see Fig. 26(b)]. All these changes become more prominent as $\Delta\phi$ moves towards π.

From the above results, it is seen that the most significant changes in the wake stability occur in the case located at the center of the primary lock-on regime, i.e., at $f_{sj}^* = 1$ and $\Delta\phi = \pi$. In this case, the disturbance growth rate monotonically decreases with x^*, instead of having a peak as in the unforced case. Also, the flow becomes convectively unstable even in the very near field between $x^* = 1.3$ and 2. This indicates that the SJ pair operating at the center of a lock-on regime is the most capable of changing the wake instability and hence the resulting dynamics. Although not presented here for brevity, the instability analyses conducted in other lock-on regimes also confirm this observation.

VI. CONCLUSIONS

This paper presents a systematic study on SJ-based active lock-on. For the first time the effect of the forcing phase difference on the characteristics of lock-on is investigated. An extended linear theory is proposed to predict the centers of various lock-on regimes in a parametric map spanned by the forcing frequency and phase difference. By satisfying Eqs. (13) and (14), discrete lock-on regime centers are identified, which are marked with cross signs in Fig. 4. It can be concluded that when the forcing frequency (f_{sj}^*) is an integer multiple (including 1) of the natural vortex shedding frequency, harmonic or subharmonic lock-on occurs at particular forcing phase differences ($\Delta\phi$). A single lock-on regime exists at each of these frequencies, whose central forcing phase difference is 0 (in phase) at even f_{sj}^* and π (in antiphase) at odd f_{sj}^*. On the other hand, when the forcing frequency is a submultiple of the natural vortex shedding frequency, superharmonic lock-on occurs at particular forcing phase differences. Multiple lock-on regimes exist at each of these frequencies: two centers in the first superharmonic lock-on regime at $f_{sj}^* = 1/2$, three centers in the second superharmonic lock-on regime at $f_{sj}^* = 1/3$, and so on. Their first centers all fall on a line $\Delta\phi = \pi f_{sj}^*$, and the remaining centers spread along the constant frequency line with an increment of $2\pi f_{sj}^*$.

To confirm the theory and also to determine the shape and size of each lock-on regime, a series of numerical simulations is conducted on a circular-cylinder flow system with external forcing realized by a pair of SJs. At a Reynolds number 100 and with moderate SJ forcing, five lock-on regimes are captured, i.e., the primary, secondary, tertiary, and first- and second-superharmonic lock-on regimes. The centers of these lock-on regimes coincide with the theory-predicted centers. Furthermore, it is found that these lock-on regimes are generally in a rhomboidal shape, and their size gradually reduces when the SJ frequency is away from the natural vortex shedding frequency.

With the simulation results, the aerodynamic forces and wake formation in various lock-on regimes are analyzed and compared. It is revealed from Fig. 5 that the occurrence of lock-on significantly affects the mean lift and drag forces, as well as the lift fluctuations, but its influence on drag fluctuations is relatively weak. As for the cylinder wakes, in general the wake's spatio-temporal symmetry still holds when the SJ frequency varies in lock-on regimes, whereas it does not hold when the SJ pair changes its phase difference. An exception is given to superharmonic lock-on regimes, however, in which varying the SJ frequency also destroys the symmetry because the SJ pair

injects momentum into the flow system once every several vortex shedding periods. The interaction between the SJ pair and the vortex development is also investigated in details through the discussion of $\Delta\phi^l$ (phase difference between the C_L peak and its nearest upper SJ velocity peak) and $\Delta\phi^u$ (phase differences between the C_L peak and its nearest lower SJ velocity peak). It is revealed that the timing of SJ blowing stroke plays an important role in the vortex development and resulting wakes.

Last, linear stability analysis is conducted on the unforced case and several selected cases in the primary lock-on regime. It is found that the SJ pair changes the wake dynamics and aerodynamics through modifying the size and disturbance growth rate of the absolutely unstable flow region that is located immediately downstream of the cylinder. Also, the SJ pair operating at the center of the lock-on regime is the most capable of making such changes.

Through this study, a better understanding in active lock-on has been achieved, which will be helpful in future exploration of lock-on-related applications.

---

[1] C. H. K. Williamson and A. Roshko, Vortex formation in the wake of an oscillating cylinder, J. Fluids Struct. **2**, 355 (1988).

[2] S. H. Kim, J. Y. Park, N. Park, J. H. Bae, and J. Y. Yoo, Direct numerical simulation of vortex synchronization due to small perturbations, J. Fluid Mech. **634**, 61 (2009).

[3] L. H. Feng and J. J. Wang, Circular cylinder vortex-synchronization control with a synthetic jet positioned at the rear stagnation point, J. Fluid Mech. **662**, 232 (2010).

[4] O. M. Griffin, Flow similitude and vortex lock-on in bluff body near wakes, Phys. Fluids A: Fluid Dyn. **1**, 697 (1989).

[5] O. M. Griffin and M. S. Hall, Review-vortex shedding lock-on and flow control in bluff body wakes, J. Fluids Eng. **113**, 526 (1991).

[6] C. H. K. Williamson and R. Govardhan, Vortex-induced vibrations, Annu. Rev. Fluid Mech. **36**, 413 (2004).

[7] T. Sarpkaya, A critical review of the intrinsic nature of vortex-induced vibrations, J. Fluids Struct. **19**, 389 (2004).

[8] R. B. Kotapati, R. Mittal, O. Marxen, F. Ham, D. You, and L. N. Cattafesta, Nonlinear dynamics and synthetic-jet-based control of a canonical separated flow, J. Fluid Mech. **654**, 65 (2010).

[9] M. Pastoor, L. Henning, B. R. Noack, R. King, and G. Tadmor, Feedback shear layer control for bluff body drag reduction, J. Fluid Mech. **608**, 161 (2008).

[10] K. Taira and T. I. M. Colonius, Three-dimensional flows around low-aspect-ratio flat-plate wings at low Reynolds numbers, J. Fluid Mech. **623**, 187 (2009).

[11] L. Du and X. Sun, Suppression of vortex-induced vibration using the rotary oscillation of a cylinder, Phys. Fluids **27**, 023603 (2015).

[12] P. M. Munday and K. Taira, On the lock-on of vortex shedding to oscillatory actuation around a circular cylinder, Phys. Fluids **25**, 013601 (2013).

[13] S. J. Baek and H. J. Sung, Quasi-periodicity in the wake of a rotationally oscillating cylinder, J. Fluid Mech. **408**, 275 (2000).

[14] S. J. Baek, S. B. Lee, and H. J. Sung, Response of a circular cylinder wake to superharmonic excitation, J. Fluid Mech. **442**, 67 (2001).

[15] M. Cheng, Y. T. Chew, and S. C. Luo, Numerical investigation of a rotationally oscillating cylinder in mean flow, J. Fluids Struct. **15**, 981 (2001).

[16] S. Kumar, C. Lopez, O. Probst, G. Francisco, D. Askari, and Y. Yang, Flow past a rotationally oscillating cylinder, J. Fluid Mech. **735**, 307 (2013).

[17] P. Sellappan and T. Pottebaum, Vortex shedding and heat transfer in rotationally oscillating cylinders, J. Fluid Mech. **748**, 549 (2014).

[18] P. K. Stansby, The locking-on of vortex shedding due to the cross-stream vibration of circular cylinders in uniform and shear flows, J. Fluid Mech. **74**, 641 (1976).

[19] P. Anagnostopoulos, Numerical study of the flow past a cylinder excited transversely to the incident stream. Part 1: Lock-in zone, hydrodynamic forces and wake geometry, J. Fluids Struct. **14**, 819 (2000).

[20] B. H. Kim and D. R. Williams, Nonlinear coupling of fluctuating drag and lift on cylinders undergoing forced oscillations, J. Fluid Mech. **559**, 335 (2006).

[21] J. S. Leontini, B. E. Stewart, M. C. Thompson, and K. Hourigan, Wake state and energy transitions of an oscillating cylinder at low Reynolds number, Phys. Fluids **18**, 067101 (2006).

[22] A. Ongoren and D. Rockwell, Flow structure from an oscillating cylinder. Part 2. Mode competition in the near wake, J. Fluid Mech. **191**, 225 (1988).

[23] T. Nishihara, S. Kaneko, and T. Watanabe, Characteristics of fluid dynamic forces acting on a circular cylinder oscillated in the streamwise direction and its wake patterns, J. Fluids Struct. **20**, 505 (2005).

[24] S. J. Xu, Y. Zhou, and M. H. Wang, A symmetric binary-vortex street behind a longitudinally oscillating cylinder, J. Fluid Mech. **556**, 27 (2006).

[25] J. S. Leontini, D. L. Jacono, and M. C. Thompson, Wake states and frequency selection of a streamwise oscillating cylinder, J. Fluid Mech. **730**, 162 (2013).

[26] J. W. Hall, S. Ziada, and D. S. Weaver, Vortex-shedding from single and tandem cylinders in the presence of applied sound, J. Fluids Struct. **18**, 741 (2003).

[27] C. Barbi, D. P. Favier, C. A. Maresca, and D. P. Telionis, Vortex shedding and lock-on of a circular cylinder in oscillatory flow, J. Fluid Mech. **170**, 527 (1986).

[28] W. Kim, J. Y. Yoo, and J. Sung, Dynamics of vortex lock-on in a perturbed cylinder wake, Phys. Fluids **18**, 074103 (2006).

[29] E. Konstantinidis and C. Liang, Dynamic response of a turbulent cylinder wake to sinusoidal inflow perturbations across the vortex lock-on range, Phys. Fluids **23**, 075102 (2011).

[30] E. Konstantinidis and D. Bouris, Vortex synchronization in the cylinder wake due to harmonic and non-harmonic perturbations, J. Fluid Mech. **804**, 248 (2016).

[31] C. Wang, H. Tang, F. Duan, and S. C. M. Yu, Control of wakes and vortex-induced vibrations of a single circular cylinder using synthetic jets, J. Fluids Struct. **60**, 160 (2016).

[32] C. H. K. Williamson, Three-dimensional wake transition, J. Fluid Mech. **328**, 345 (1996).

[33] C. Wang, H. Tang, S. C. M. Yu, and F. Duan, Active control of vortex-induced vibrations of a circular cylinder using windward-suction-leeward-blowing actuation, Phys. Fluids **28**, 053601 (2016).

[34] C. Wang, H. Tang, S. C. M. Yu, and F. Duan, Control of vortex-induced vibration using a pair of synthetic jets: Influence of active lock-on, Phys. Fluids **29**, 083602 (2017).

[35] P. Lallemand and L. S. Luo, Theory of the lattice Boltzmann method: Dispersion, dissipation, isotropy, Galilean invariance, and stability, Phys. Rev. E **61**, 6546 (2000).

[36] D. Yu, R. Mei, and W. Shyy, A multi-block lattice Boltzmann method for viscous fluid flows, Int. J. Numer. Methods Fluids **39**, 99 (2002).

[37] P. Lallemand and L. S. Luo, Lattice Boltzmann method for moving boundaries, J. Comput. Phys. **184**, 406 (2003).

[38] Y. Chen, Q. Cai, Z. Xia, M. Wang, and S. Chen, Momentum-exchange method in lattice Boltzmann simulations of particle-fluid interactions, Phys. Rev. E **88**, 013303 (2013).

[39] S. Izquierdo and N. Fueyo, Characteristic nonreflecting boundary conditions for open boundaries in lattice Boltzmann methods, Phys. Rev. E **78**, 046707 (2008).

[40] J. Zhou, R. J. Adrian, S. Balachandar, and T. M. Kendall, Mechanisms for generating coherent packets of hairpin vortices in channel flow, J. Fluid Mech. **387**, 353 (1999).

[41] T. Jardin and Y. Bury, Lagrangian and spectral analysis of the forced flow past a circular cylinder using pulsed tangential jets, J. Fluid Mech. **696**, 285 (2012).

[42] See Supplemental Material at http://link.aps.org/supplemental/10.1103/PhysRevFluids.2.104701 for the movies of the case with $f_{sj}^* = 0.8$ and $\Delta\phi = \pi$; the case with $f_{sj}^* = 1$ and $\Delta\phi = \pi$; the case with $f_{sj}^* = 1$ and $\Delta\phi = 0.5\pi$; the case with $f_{sj}^* = 2$ and $\Delta\phi = 0$ as well as the case with $f_{sj}^* = 0.5$ and $\Delta\phi = 0.5\pi$.

[43] W. Gu, C. Chyu, and D. Rockwell, Timing of vortex formation from an oscillating cylinder, Phys. Fluids **6**, 3677 (1994).

[44] S. J. Baek and H. J. Sung, Numerical simulation of the flow behind a rotary oscillating circular cylinder, Phys. Fluids **10**, 869 (1998).

[45] R. Godoy-Diana, C. Marais, J. L. Aider, and J. E. Wesfreid, A model for the symmetry breaking of the reverse Bénard–von Kármán vortex street produced by a flapping foil, J. Fluid Mech. **622**, 23 (2009).

[46] G. S. Triantafyllou, K. Kupfer, and A. Bers, Absolute Instabilities and Self-Sustained Oscillations in the Wake of Circular Cylinders, Phys. Rev. Lett. **59**, 1914 (1987).

[47] P. Huerre and P. A. Monkewitz, Local and global instabilities in spatially developing flows, Annu. Rev. Fluid Mech. **22**, 473 (1990).

[48] D. Sipp and A. Lebedev, Global stability of base and mean flows: A general approach and its applications to cylinder and open cavity flows, J. Fluid Mech. **593**, 333 (2007).

[49] B. Thiria and J. E. Wesfreid, Stability properties of forced wakes, J. Fluid Mech. **579**, 137 (2007).

[50] P. J. Schmid and D. S. Henningson, *Stability and Transition in Shear Flows*, Vol. 142 (Springer Science & Business Media, New York, 2012).

[51] K. Kupfer, A. Bers, and A. K. Ram, The cusp map in the complex-frequency plane for absolute instabilities, Phys. Fluids **30**, 3075 (1987).